

The Oxygen Features in Type Ia Supernovae and the Implications for the Nature of Thermonuclear Explosions

Xulin Zhao^{1,2}, Keiichi Maeda^{2,3}, Xiaofeng Wang¹, Lifan Wang⁴, Hanna Sai¹, Jujia Zhang⁵, Tianmeng Zhang⁶, Fang Huang¹, and Liming Rui¹

ABSTRACT

The absorption feature O I $\lambda 7773$ is an important spectral indicator for type Ia supernovae (SNe Ia) that can be used to trace the unburned material at outer layers of the exploding white dwarf. In this work, we use a large sample of SNe Ia to examine this absorption at early phases (i.e., $-13 \text{ days} \lesssim t \lesssim -7 \text{ days}$), and make comparisons with the absorption features of Si II $\lambda 6355$ and Ca II near-infrared (NIR) triplet. We show that for a subgroup of spectroscopically normal SNe with normal photospheric velocities (i.e., $v_{si} \lesssim 12,500 \text{ km s}^{-1}$ at optical maximum), the line strength of high velocity feature (HVF) of O I is inversely correlated with that of Si II (or Ca II), and this feature also shows a negative correlation with the luminosity of SNe Ia. This finding, together with other features we find for the O I HVF, reveal that for this subgroup of SNe Ia explosive oxygen burning occurs at the outermost layer of supernova and difference in burning there could lead to the observed diversity, which are in remarkable agreement with the popular delayed-detonation model of Chandrasekhar mass WD.

Subject headings: supernova: general - methods: data analysis - techniques: spectroscopic

1. Introduction

Type Ia supernovae (SNe Ia) are important in cosmology and astrophysics, not only for the key roles that they played in the discovery of accelerating universe (Riess et al. 1998; Perlmutter

¹Physics Department and Tsinghua Center for Astrophysics, Tsinghua University, Beijing, 100084, China: wang_xf@mail.tsinghua.edu.cn; zhaoxl11@mails.tsinghua.edu.cn

²Department of Astronomy, Kyoto University, Kitashirakawa-Oiwake-cho, Sakyo-ku, Kyoto 606-8502, Japan: keiichi.maeda@kusastro.kyoto-u.ac.jp

³Kavli Institute for the Physics and Mathematics of the Universe (WPI), University of Tokyo, 5-1-5 Kashiwanoha, Kashiwa, Chiba 277-8583, Japan.

⁴Mitchell Institute for Fundamental Physics and Astronomy, Texas A&M University, College Station, TX 77843, USA

⁵Yunnan Astronomical Observatory of China, Chinese Academy of Sciences, Kunming, 650011, China

⁶National Astronomical Observatory of China, Chinese Academy of Sciences, Beijing, 100012, China

et al. 1999), but also for their contribution to production of heavy elements in the Universe. However, the nature of their progenitor systems is still controversial (e.g., Maoz et al. 2014, and references therein). It is widely accepted that SNe Ia are a result of a thermonuclear explosion of carbon oxygen (C/O) white dwarfs (WDs), but there are two major channels proposed so far that could lead to such an explosion. One is an explosion of a WD which accretes hydrogen or helium from its non-degenerate companion (single degenerate scenario, Whelan & Iben 1973; Nomoto 1982; Nomoto et al. 1997), with supporting evidences from the detections of circumstellar material (CSM) around some SNe Ia (Hamuy et al. 2003; Aldering et al. 2006; Patat et al. 2007; Sternberg et al. 2011; Dilday et al. 2012; Maguire et al. 2013; Silverman et al. 2013). The other is a merger of two WDs (double degenerate scenario: Iben & Tutukov 1984; Webbink 1984), which has recently gained special attention due to the observational findings that there are no companion signature found for some SNe Ia, i.e., the nearby object SN 2011fe and some supernova remnants such as SN 1006 and SNR 0509-67.5 in LMC, down to the luminosities much fainter than the Sun (Li et al. 2011; Bloom et al. 2012; Brown et al. 2012; Hernández et al. 2012; Schaefer & Pagnotta 2012).

There are also diversities in spectroscopic and photometric properties of SNe Ia, and it has been discussed whether all (or spectroscopically normal) SNe Ia are originated in a single evolutionary path or there are multiple populations. For example, there is a so-called high velocity (HV) subclass of SNe Ia (Wang et al. 2008, 2009a), with redder peak $B - V$ colors and slower late-time decline rates in bluer bands relative to the normal velocity (Normal) subclass¹, and it is interesting to explore whether they represent different populations. The observed differences between the HV and Normal SNe Ia could be at least partly attributed to be a geometric effect of an asymmetric explosion (Maeda et al. 2010; Maund et al. 2010). However, such observed diversities are also found to be linked to their birthplace environments to some extent (Wang et al. 2013), suggesting that SNe Ia may arise from multiple classes of binary evolution. Taking together, it could mean that there are two populations in the HV subclass in which one is related to the Normal SNe Ia while the other is not.

The other long-standing problem is the physical process of SN Ia explosions (Hillebrandt & Niemeyer 2000). Theoretically, the thermonuclear reaction disrupting the star may propagate at a range of speeds from subsonic deflagration to supersonic detonation (Nomoto et al. 1984; Khokhlov 1991; Fink et al. 2010; Pakmor et al. 2012). The most popular scenario is the delayed-detonation model (Khokhlov 1991) which assumes that a strong detonation unbinds the whole progenitor WD, after a deflagration which produces stable Fe-peak elements near the center of the WD. Another popular model involves the double-detonation mechanism (Livne & Glasner 1990; Fink et al. 2007; Sim et al. 2012; Shen & Bildsten 2014). In this model, explosive He burning is induced on the WD surface by compressional heating if the accreted He amount is sufficiently large, and

¹This spectroscopic classification is based on the photospheric velocity measured from Si II λ 6355 lines in the near-maximum-light spectra (Wang et al. 2009a).

this creates a shock-wave penetrating into the WD core. Once the shock wave is converged near the center, a powerful detonation can be triggered and it will lead to the explosion unbinding the whole WD. Existing observational diagnostics offer some clues to the explosion models, while this topic is still controversial.

The high-velocity absorption features (HVF) can provide clues to the burning processes in the outer layers of the exploding WD, though their origins are still debated. This is a high-velocity ($>16,000 \text{ km s}^{-1}$) component that is likely formed in regions lying above the photosphere (Hatano et al. 1999; Mazzali et al. 2005a). The HVFs of Ca II near-infrared (NIR) triplet and Si II 6355 Å in SNe Ia have been systematically examined using both early-phase and near-maximum-light spectra (Maguire et al. 2012; Childress et al. 2014; Silverman et al. 2015; Zhao et al. 2015). These studies indicate that the abundance distributions of Si and Ca are strongly related, likely as a result of the same burning process responsible to create Si and Ca. Since Si and Ca are produced basically in the same burning layer, their relative strengths are not expected to be sensitive to the typical burning process they experienced. It is thus interesting to make comparisons with absorption features created by elements whose abundance pattern is different from Si and Ca in different burning layers. The C II $\lambda 6580$ could be an important indicator of unburned fuel in the progenitor and the observations of this feature have been discussed in many literatures (Thomas et al. 2011; Parrent et al. 2011; Blondin et al. 2012; Folatelli et al. 2012; Silverman et al. 2012d; Maguire et al. 2014; Hsiao et al. 2015). However, the C II $\lambda 6580$ absorption is usually very weak and difficult to be quantified in line strength and velocity distribution. On the other hand, the O I $\lambda 7773$ line is relatively strong but not explored so far. We thus propose using this feature as a tracer of unburned materials in this paper, although part of oxygen is also produced via carbon burning.

The presence of HVF in O I $\lambda 7773$ absorption was only reported in the earliest spectra of SN 2011fe in M101 but it was observed to disappear rapidly (Nugent et al. 2011). Detection of such an O-HVF is critically important, since Si and Ca are produced from O via the oxygen burning, and the comparison between the HVF of O and those of Si and Ca can be potentially used to confirm their associations. In the Si burning layer, the oxygen is fully consumed; in the O burning layer, all the O, Si, and Ca can have large abundances; in the C burning layer, the oxygen is abundant but the Si and Ca are under-abundant; and finally in the unburned layer again, the ratio of O to Si or Ca is large. Therefore, we may obtain information about the typical burning process encountered by the layer producing the HVFs, and hence the still-unclarified origin of the outermost materials in SN Ia.

This paper is organized as follows. In §2, our data samples and the methods for measuring the spectral parameters are introduced. In §3, correlations between spectroscopic parameters of oxygen (O I $\lambda 7773$) and those of other elements (Si II $\lambda 6355$, Ca II NIR triplet, and C II $\lambda 6580$) are investigated. Correlations between spectroscopic features of O I $\lambda 7773$, Si II $\lambda 6355$, Ca II NIR triplet and luminosity indicator $\Delta m_{15}(B)$ are also examined and analyzed in this section. Origins of the high velocity features and the constraints on the explosion models are discussed in §4. The

paper is closed in §5.

2. Dataset and Methods of Measurement

2.1. Sample

Since the HVFs of SNe Ia are only prominent in their early spectra, we choose the sample with spectroscopic observations at $t \lesssim -7$ days from the B-band maximum light. From the published spectral database from the CfA supernova program (Matheson et al. 2008; Blondin et al. 2012), the Berkeley supernova program (Silverman et al. 2012a), Carnegie Supernova Project (CSP: Folatelli et al. 2013), and the unpublished dataset from the Tsinghua supernova program². The telluric absorption features were removed from almost all of the above spectral sample using the standard-star spectra obtained with the same slit used for the SN observations. Nevertheless, this procedure often leaves residuals from the strongest telluric bands near 7620\AA . With the multi-gaussian fit addressed in next subsection, we examine the blending of the residual telluric absorption with the O I $\lambda 7773$ absorption in the spectra of our SN Ia sample. Those spectra showing larger degrees of blending between these two absorptions (see §2.2) are excluded in our analysis. Moreover, the near-maximum-light Si II $\lambda 6355$ velocity is also required for further classification of our sample. This leads to a total of 143 early-time spectra (with $t \lesssim -7$ days from the B-band maximum light) that cover the wavelength region of O I $\lambda 7773$ absorption. These spectra belong to 62 SNe Ia, including 55 spectroscopically normal SNe Ia, 2 SN 1991T-like (Filippenko et al. 1992; Phillips et al. 1992) and 5 SN 1999aa-like SN Ia (Li et al. 2001) (hereafter these two subclasses are abbreviated to 91T/99aa-like SNe Ia). The spectroscopically normal objects can be further divided into 42 Normal SNe Ia and 13 HV ones.

The above sample of SNe Ia are mostly included in our previous study (Zhao et al. 2015), where their photometric and host-galaxy parameters (i.e., $\Delta m_{15}(B)$, $B_{max} - V_{max}$, spectroscopic subclassification, host-galaxy type, K -band magnitude of the host galaxy etc.) can be found. The sources of the light curves are from the Harvard CfA SN group (Hicken et al. 2009, 2012), the CSP (Contreras et al. 2010; Stritzinger et al. 2011), the Lick Observatory Supernova Search (LOSS: Ganeshalingam et al. 2010), and our own database.

2.2. Measurement Procedure

The measurement procedure of O I absorption is overall similar to that applied to measuring the Si II 6355/5972 and Ca II near infrared (NIR) triplet absorptions (Zhao et al. 2015), but

²This dataset contains nearly 1000 spectra for over 200 SNe (Rui et al. in preparation), obtained with the Lijiang 2.4-m telescope (+YFOSC) of Yunnan Astronomical Observatories and the Xinglong 2.16-m telescope (+BFOSC) of National Astronomical Observatories of China.

with more gaussian components being used to fit more absorptions. The absorptions identified around O I $\lambda 7773$ include three O I components (two high-velocity features and one photospheric component), three residual telluric components (i.e., at λ s 7186, 7606, 7630Å), and a possible Mg II $\lambda 7890$ (with a velocity at $10,000 \text{ km s}^{-1} \sim 14,000 \text{ km s}^{-1}$). These absorption components can be represented using the following multi-component Gaussian function:

$$f(\lambda) = \sum_{i=1}^6 A_i \exp\left(-\frac{(\lambda_i - \lambda_i^0)^2}{2\sigma_i^2}\right) \quad (1)$$

where subscript $i=1-6$ denote the PHO component of O I $\lambda 7773$, the "main" HVF (hereafter HVF-I), the possible "second" HVF (hereafter HVF-II), and the telluric absorptions at 7168Å, 7605Å and 7630Å, respectively. In the above equation, A_i is the amplitude (i.e., the maximum absorption), σ_i is the dispersion (i.e., the standard deviation in a normal distribution), and λ_i^0 is the laboratory wavelength of specific spectral line. Note that the positions of the telluric absorptions (and thereby the λ_i^0) are blueshifted relative to the rest-frame wavelengths due to that the spectrum was corrected for the redshift of the host galaxy.

In the fitting, the pseudo-continuum is defined as a straight line connecting the line wings on both sides of the absorption, which is determined through repeated visual inspections and careful manual adjustments in order to better counter the noise. As usual, the line strength of an absorption feature is quantified by the pseudo-equivalent width (pEW). From equation 1, we have:

$$pEW = \sum \sqrt{2\pi} A_i \sigma_i \quad (2)$$

where the summation is performed for appropriate components.

Before fitting, we smoothed the observed spectrum around the O I $\lambda 7773$ absorption (i.e., covering the wavelength range from 7000 to 7800Å) with a locally weighted scatter-plot smoothing method (Cleveland 1979) in order to reduce the effect of noise spikes on the fitting results, as the O I $\lambda 7773$ line (especially the high-velocity feature) is usually weak in early-time spectra of SNe Ia. In our previous work (Zhao et al. 2015), the PHO velocity Si II 5972 was used as an initial condition to constrain that of Si II $\lambda 6355$ because the HVF and PHO component of the latter feature are often seriously blended. In determining the velocity of O I $\lambda 7773$ line, however, we did not use the velocity condition from Si II $\lambda 5972$ or Ca II NIR triplet lines because the HVF feature and PHO component of O I $\lambda 7773$ line are distinctly separated (i.e., by about 6000 km s^{-1}) and their locations can be better determined in early time spectra, as shown in Figure 1. The only exceptions are for several HV SNe Ia where their HVF and PHO components show **more severe blending** (i.e., SN 2002dj) and the velocity of Si II $\lambda 5972$ is used to help better locate the PHO component of O I $\lambda 7773$.

As most of the published spectral data do not have the accompanied flux errors, we adopt the R -squared statistic to fit the parameters of absorption features such as the amplitude A_i , the dispersion σ_i , and velocity of absorption minima v_i^0 . This fitting procedure is done through the Curve Fitting Toolbox in Matalab, where regression analysis can be conducted using the library

of various models provided. Generally speaking, the fittings were well-performed and objectively determined by the absorption profiles, with the typical R -squared value being 0.97 for our sample. There are some reasons that the multiple gaussian fitting applied in our analysis can be well done without over/under-fitting. Firstly, the blending between HVFs and PHO components of O I $\lambda 7773$ is much weaker than that seen in Si II $\lambda 6355$ or Ca II NIR triplet. Secondly, the contaminations from residual telluric absorptions are not very serious for our selected sample. For example, the blending ratio between the telluric absorption and the photospheric component of O I $\lambda 7773$ is overall small for our sample (see discussions below). Thirdly, in most cases, the possible Mg II $\lambda 7890$ is not strong (with pEW $\lesssim 10\text{\AA}$) and it is well separated from the PHO component of O I $\lambda 7773$.

Figure 1 shows the absorption features centering at O I $\lambda 7773$ in the $t \approx -10$ days spectra of some representative SNe Ia. Demonstration of applying multiple-gaussian fit is shown in the plot, where the photospheric (PHO) absorption of O I $\lambda 7773$ (at $\sim 12,000 \text{ km s}^{-1}$) is accompanied by two additional absorptions on the blue side. These two absorptions can be attributed to the HVF-I and HVF-II of oxygen at velocities $\sim 18,000 \text{ km s}^{-1}$ and $\sim 22,000 \text{ km s}^{-1}$, respectively, and this identification is secured by comparisons with the SYNOW fit as shown in Figure 2 (Fisher et al. 1995). We notice that different absorption components of O I line are clearly separated from each other for Normal SNe Ia, while the O-HVF absorptions tend to blend with the PHO component in some HV SNe Ia such as SN 2002bo and SN 2002dj.

In this work, errors of spectral fit were retrieved from the Matlab function "confint". This function calculates the confidence bounds of the fitting results using $t\sqrt{((X^T X)^{-1} s^2)}$, where X is the Jacobian of fitted values, X^T is the transpose of X , s^2 is the mean squared error, and t is calculated using the inverse of Student's cumulative distribution function. The errors of A_i and σ_i are then used to compute that of the pEW using Eq.(2), and the error of λ_i is converted to that of the line velocity. Since the fitting is applied to the smoothed spectrum, the noise of original spectrum is further factored into the above errors by taking residual standard deviation between the original and smoothed data roughly as $1\text{-}\sigma$ error in spectral fitting. The typical error from spectral noise is about 3% for our sample, and the corresponding error in pEW is about 1.0\AA . Additional velocity error is also considered for the fits to the smoothed spectra, which is taken to be velocity shift from gaussian fits to the smoothed and original spectra³ or the standard error of these two fits (i.e., 460 km s^{-1} for the PHO component and 515 km s^{-1} for the HVF for 87 spectra) when the Matlab code fails to fit the original spectra. Moreover, the photospheric component of O I $\lambda 7773$ absorption might be also affected by the residual telluric absorptions. To get a quantitative estimation of this contamination, we introduce a parameter of blending ratio R_b which measures the fraction that the line profile of the PHO component of O I $\lambda 7773$ is overlapped by the telluric

³The fit to the original spectra can be done for 87 of 143 for our sample. The resultant velocities (and pEW) are well consistent with those from fits to the smoothed spectra, with the adjusted R-squared coefficient for linear correlations being 0.91 for the PHO component and 0.83 for the O-HVF component, respectively.

absorption. This ratio is calculated as $\text{pEW}_{\text{blending}}^{\text{telluric}}/\text{pEW}_{\text{PHO}}^{\text{O}}$, where $\text{pEW}_{\text{blending}}^{\text{telluric}}$ represents the pEW of the region of telluric feature that is blended with the PHO component of O I $\lambda 7773$ and $\text{pEW}_{\text{PHO}}^{\text{O}}$ refers to the pEW of the O-PHO. Results of this parameter measured for each spectrum of our sample are reported in the last column of Table 2. Such a blending ratio is overall small for our sample, with a mean value of only 3.7%, suggesting that the effect of residual telluric lines be negligible. Besides the uncertainties listed above, the PHO component of O I $\lambda 7773$ could also suffer from blending of an unknown component that could be due to Mg II $\lambda 7890$ or additional absorption feature of oxygen at lower velocities (i.e., $<7,000 \text{ km s}^{-1}$). However, these two effects are not considered in this work because they are difficult to be quantified.

2.3. Temporal Evolution of O I $\lambda 7773$

The temporal evolution of the line velocity and strength of O I $\lambda 7773$ absorption is shown in Figure 3 for some well-observed SNe Ia, including SNe 2002dj, 2005cf, 2009ig, 2011fe, 2012fr, and 2013dy (see Table 1 for references). According to the spectroscopic classification as proposed by Wang et al. (2009a), SN 2002dj and SN 2009ig belong to the HV subclass of SNe Ia, while SN 2005cf, SN 2011fe, and SN 2013dy can be put into the Normal subclass. SN 2012cg shares some properties similarly seen in the SN 1999aa-like subclass that is characterized by shallow silicon in the spectra (Silverman et al. 2012b; Zhang et al. 2014; Marion et al. 2015). SN 2012fr may lie at the boundary of the above classifications (Zhang et al. 2014).

As shown in the left panels of Figure 3, the O I $\lambda 7773$ absorption of different SNe Ia shows large differences in the velocity and the velocity evolution for both the HVF and PHO components. For example, at $t \approx -10$ days, the PHO velocity measured for our sample has a range from $\sim 11,000 \text{ km s}^{-1}$ to $\sim 15,000 \text{ km s}^{-1}$, and the velocity of the HVF-I ranges from $\sim 17,000 \text{ km s}^{-1}$ to $\sim 20,000 \text{ km s}^{-1}$. The O I line (both PHO and HVF-I) of the HV SNe Ia has a velocity that is on average larger than that of the Normal ones by $3000\text{-}4000 \text{ km s}^{-1}$ at comparable phases, as is similar to the case seen in Si II $\lambda 6355$ (Zhao et al. 2015). Restricting the data to the phases from $t \sim -13$ days to $t \sim -7$ days in the calculations of velocity gradient, we find that the velocity gradient measured for the PHO components of SN 2005cf, SN 2011fe, and SN 2013dy is -182 , -186 , and $-100 \text{ km s}^{-1} \text{ d}^{-1}$, respectively, while the corresponding values obtained for their HVFs are -183 , -227 , and $-263 \text{ km s}^{-1} \text{ d}^{-1}$. For SN 2002dj, SN 2009ig, SN 2012cg, and SN 2012fr, the velocity gradient of the PHO component is -379 , -199 , -329 , and $-257 \text{ km s}^{-1} \text{ d}^{-1}$, while the corresponding value for the HVF is -134 , -644 , -136 , and $-413 \text{ km s}^{-1} \text{ d}^{-1}$. The Normal SNe Ia appear to have relatively uniform velocity evolution compared to other subclasses of SNe Ia. This may enable better extrapolations of absorption velocity to the value at a given phase (i.e., $t \sim -10$ days) for some normal sample when necessary. By contrast, the velocity evolution shown by SN 2002dj and SN 2009ig show large scatter either for the HVF or the PHO component, which may be more or less due to that the HV SNe Ia suffer more serious line blending and it is difficult to separate the HVFs from the PHO components.

The strength of the O I $\lambda 7773$ absorption is plotted as a function of phase in the right panels of Figure 3, which shows even larger scatter than the velocity. One can see that the O I absorptions are found to be strong in some SNe Ia such as SN 2002dj and SN 2011fe but they are marginally detected in other objects such as SN 2009ig and SN 2012fr. Note, however, that the absorption strength of the O-HVF does not show significant variations with time for our sample, especially the Normal subsample. This is different from the trend seen in the HVFs of Si II $\lambda 6355$ line and Ca II NIR triplet, which become weak at a faster pace perhaps due to having optically thin environment in outermost layers (see the references in Zhao et al. 2015).

3. Statistical Analysis

Table 1 lists the line velocities and strengths of O I $\lambda 7773$, Si II $\lambda 6355$, Ca II NIR triplet, and C II $\lambda 6580$ absorptions obtained at $t \sim -10$ days for 62 SNe Ia. If, however, more than one spectra are available during the period from $t = -11$ days to $t = -9$ days, the median values are presented. The B-band light-curve decline rate $\Delta m_{15}(B)$ (Phillips 1993) is also listed. The detailed results about the measurements of velocities and pEW of the O I $\lambda 7773$ and C II $\lambda 6580$ absorptions at different phases are tabulated in Tables 2 and 3. Given the uncertainties due to line blending and/or intrinsically larger scatter in temporal evolution of O I absorption for HV SNe Ia, we concentrate on the spectroscopically normal SNe Ia with $v_0^{Si} < 12,500 \text{ km s}^{-1}$ in the following analysis.

3.1. Expansion Velocity from O I 7773

Velocity distribution of the ejected matter at different layers of the exploding WD can provide strong constraints on its compositional structure. To get an overall picture of velocity distribution of C II $\lambda 6580$, Si II $\lambda 6355$, O I $\lambda 7773$, Ca II NIR triplet, we construct the mean spectrum using spectra of a subsample of Normal SNe Ia whose spectra have a sufficiently high signal-to-noise (S/N) ratio (i.e, $S/N \gtrsim 20$) and cover phases close to $t = -10$ days. The mean profiles of the above four absorption features are shown in Figure 4, where the Ca II lines are characterized by prominent HVFs at $\sim 22,000 \text{ km s}^{-1}$ and the O I line is characterized by the HVF-I at $\sim 18,000 \text{ km s}^{-1}$ and the possible HVF-II at $\sim 22,000 \text{ km s}^{-1}$. The small notch on the blue side of Si II $\lambda 6355$ absorption corresponds to the HVF of Si formed at a velocity of about $18,000 \text{ km s}^{-1}$. The C II $\lambda 6580$ absorption does not show any significant signature of absorption feature at high velocity. As it can be seen, the photospheric components of different species have similar velocities (see blue dashed line in Figure 4). Note that Figure 4 is constructed for illustrative purpose only.

Figure 5 shows the expansion velocities measured from absorption minima of Si II, Ca II, and C II lines versus that from the O I line. At the photospheric layer, the velocity of O I line shows a positive correlation with that of Si II, Ca II, and C II lines; and a linear fit indicates that the O I

velocity is slightly lower than the Si II and C II velocities by about 750 km s^{-1} . At outer layers, the HVF-I of O (referred as O-HVF for short) shows a similar but slightly lower central velocity compared to the Si-HVF; and at very outer layers, the HVF-II of O has a velocity that is roughly comparable to the Ca-HVFs. This similarity in expansion velocity indicates that the fuel-indicative O and the burned Si (or Ca) are physically connected. The observation results for the small velocity differences between them and that the Ca-HVFs have higher velocities relative to the Si-HVF might be well explained by different ionization (or excitation) energies required to produce lines of O I $\lambda 7773$ (i.e., $E_{ex} = 9.15 \text{ eV}$), Si II $\lambda 6355$ (i.e., $E_{ex} = 8.12 \text{ eV}$), and Ca II NIR triplet (i.e., $E_{ex} = 1.7 \text{ eV}$). For a relatively low temperature expected for the outermost HVF-forming layer, Ca II NIR triplet are more easily formed and saturated compared to the Si II and O I lines.

3.2. Equivalent Width of O I 7773

The line strength of O I 7773 absorption carries important information on the diversity of SNe Ia. Figure 6 shows the pEW (PHO and HVF) of O I absorption versus the corresponding velocities, measured from the $t \approx -10$ day spectra of our SN Ia sample. As can be readily seen in these figures, these two quantities do not show significant correlation for the full sample, as indicated by the lower Pearson coefficients. Excluding the HV SNe Ia from the statistical sample, a modest anti-correlation seems to emerge between the pEW and velocity of O I lines, though there are a few outliers. These results indicate that a smaller amount of oxygen is detected in SNe Ia with relatively larger expansion velocities. Such an inverse relation becomes stronger for the subsample with prominent detection of C II $\lambda 6580$ absorption, i.e., $\text{pEW} \gtrsim 1.0 \text{ \AA}$ at $t \approx -10$ days (see table 3 for the detailed results of the measurements). And the corresponding Pearson coefficients ρ are -0.64 and -0.67 for the correlations of the HVF and PHO components, respectively. The much tighter pEW-velocity relation for O I $\lambda 7773$ absorption suggests that the SNe Ia showing prominent carbon in spectra may form a distinct population with relatively smaller diversity.

We notice that the velocity-pEW correlation seen in O I $\lambda 7773$ absorption is contrary to that seen in Si II $\lambda 6355$ line (Wang et al. 2009a; Blondin et al. 2012), which directly reflects the different roles that O and Si play in the burning in the HVF and photospheric layers. In the rightmost panel of Figure 6, we further examined the relation between the absorption strengths of the HVF and PHO components of O I $\lambda 7773$. We find that the pEW of the O-HVF absorption is highly correlated with that of the O-PHO absorption, which has a Pearson coefficient of 0.86. This strong correlation indicates that the O detected at very outer layers of the ejecta is intrinsic to the SNe, rather than from other sources such as CSM, which usually lies far outside the exploding WD and should not have such a strong connection with the photosphere unless the CSM properties is somehow tied with SN properties. Note that the O-HVF we discussed here refers to the HVF-I marked in Figure 1, and we did not attempt to quantify the correlations of the HVF-II of O with the HVFs of Si (or Ca) because this feature is usually very weak and there are relatively larger uncertainties in measuring its absorption strength.

3.3. Correlations of O I $\lambda 7773$, Si II $\lambda 6355$, and Ca II NIR triplet

In our previous study, HVFs of both Si II $\lambda 6355$ and Ca II NIR triplet in SNe Ia were systematically examined using their early-phase spectra. While the PHO velocity was found to be similar between Si II $\lambda 6355$ and Ca II NIR triplet, the HVF velocity of the latter is higher than the former by about $4,000 \text{ km s}^{-1}$. Similarly, although Ca II NIR triplet has a PHO strength that is roughly comparable to the Si II $\lambda 6355$, its HVF is found to be much stronger (by about 6 times). Note that these correlations are all positive, meaning that the velocity and strength of these two lines grow/decline in the same direction. These two spectral lines were also found to show similar behaviors as functions of photometric and host-galaxy properties like $\Delta m_{15}(B)$, $B_{max} - V_{max}$ color, host-galaxy type etc. (see details in Zhao et al. 2015). These results indicate that the amount of Si and Ca in both PHO- and HVF-forming regions are strongly connected. Nevertheless, the ratio of Si to Ca is not sensitive to different burning processes expected in SNe Ia (indeed which is similar to the unburned solar composition), while the ratio of O to Si (or Ca) is expected to be quite different in different layers.

Figure 7 compares the line strengths of O and Si for our sample of SNe Ia. From the left panel of the plot, one can see that the PHO components of O and Si are positively correlated and the Pearson coefficient is 0.69 for the Normal SNe Ia. On average, the pEW of O-PHO absorption is found to be roughly 1/3 times that of the Si II. Inspection of the right panel of Figure 7, however, reveals that there is a distinct anti-correlation between the absorption strengths of the HVFs of Normal SNe Ia, with the Pearson coefficient $\rho = -0.71$ for a linear relation. Assuming a reciprocal correlation for pEW $_{HVF}^O$ - pEW $_{HVF}^{Si}$ relation, the Pearson coefficient becomes 0.90. Similar correlation (for the PHO component) and anti-correlation (for the HVF) can be also found between the line strengths of O I $\lambda 7773$ and Ca II NIR triplet lines as shown in Figure 8, though both these relations are less significant. Compared to Normal SNe Ia, the HV ones (i.e., $v_0^{Si} \gtrsim 12500 \text{ km s}^{-1}$) show large scatter in both Figure 7 and Figure 8, and do not seem to follow well the above relations in particular the anti-correlation of the HVFs. The spectroscopically peculiar and luminous objects, with weak absorptions of both O and Si, also show obvious deviations in the plots of the HVFs.

The anti pEW $_{HVF}^O$ - pEW $_{HVF}^{Si}$ correlation indicates that, at very outer layers of the exploding WD, less amount of O will be detected when there are more abundant of Si and Ca, and this favors the need for the oxygen burning to produce those HVFs. Again the HV subgroup of SNe Ia are found to show larger scatter in this correlation, suggesting that their HVFs may have different origins (see discussions in §4).

3.4. Correlation of the Absorption with Peak Luminosity

Since the line velocity and strength of O I 7773 absorption feature shows a wide range for different SNe Ia, it is necessary to explore the reasons for this diversity. Peak luminosity is an

important parameter reflecting the properties of SNe Ia. In Figure 9, the observed features of O-PHO and O-HVF (including both line velocity and absorption strength) are plotted against the luminosity-indicator parameter $\Delta m_{15}(B)$. As it is readily seen, the velocity of the O-HVF shows a modest dependence on $\Delta m_{15}(B)$, with slower-declining (or more luminous) SNe Ia having larger ejecta velocities at outer layers. This velocity-luminosity relation can be explained if the characteristic velocity is moved toward higher velocities for explosions with more complete burning. Due to the loss of absorbing oxygen material, the strength of the absorption feature could then be weakened for SNe Ia with higher luminosities. This is supported by the prominent pEW - $\Delta m_{15}(B)$ relation as shown in the right panels of Figure 9, where stronger O I absorptions are found in SNe Ia with lower luminosities. On average, the SNe Ia with $\Delta m_{15}(B) \gtrsim 1.20$ mag have pEWs that are about 2.0 times larger than those with $\Delta m_{15}(B) < 1.20$ mag. The above relations become **stronger** when the HV SNe Ia are discarded in the analysis.

As a comparison, the correlations of Si-HVF and Ca-HVF (line strength and velocity) with $\Delta m_{15}(B)$ are also examined in Figure 10. The velocities of Si- and Ca-HVF are also found to be lower for SNe Ia with larger decline rates, which is similar to the behavior shown by the O-HVF. Although the strength of Si-HVF does not show a strong anti-correlation with $\Delta m_{15}(B)$, it is clear that stronger Si-HVF tends to be detected in more luminous SNe Ia (i.e., with $\Delta m_{15}(B) < 1.3$ mag). This tendency is consistent with the earlier result obtained using the relative line strength of the Si- and Ca-HVFs (Childress et al. 2014; Silverman et al. 2015; Zhao et al. 2015). The correlation between Si-HVF and $\Delta m_{15}(B)$ is weaker than that observed between O-HVF and $\Delta m_{15}(B)$, which can be due to that not all luminous SNe Ia have prominent Si-HVF and the line blending of the HVF and the photospheric component is more serious than that for the O I $\lambda 7773$ absorption. The fact that the Si-HVF and O-HVF show an opposite correlation with Δm_{15} suggests that ionization effect should not play a key role in forming the HVFs in the outer layers of the ejecta since Si and O have similar ionization energy (see detailed discussions in §4.1).

4. Discussions

4.1. Origin of the High Velocity Features

The origin of HVFs in SNe Ia still remains unclear. It has been suggested that HVFs could be associated with abundance enhancement (AE), density enhancement (DE) or ionization enhancement (IE) in the outermost layers (Gerardy et al. 2004; Mazzali et al. 2005a,b; Blondin et al. 2012). The material producing the HVFs could be either intrinsic to the SNe or from the CSM. The features we investigate in this work, i.e., O I $\lambda 7773$, Si II $\lambda 6355$ and Ca II NIR triplet are suited to probe density structure (through pEW), velocity distribution (see Figure 4), and composition (through pEW) of the ejecta. With these information, we may decode the main functions involved in the origin of some HVFs.

Here we briefly summarize these scenarios so far proposed for the formation of HVFs. In the

AE scenario, the abundances of Si and Ca are somehow enhanced in the outermost regions of the ejecta. A possible cause is a strong asymmetry in the explosion process (see Maeda et al. 2010 and Seitenzahl et al. 2013 for SD scenario, or Röpke et al. 2012 for DD scenario). Alternatively, the abundances could be enhanced by the He-burning near the WD surface, as suggested by double-detonation model (e.g., Fink et al. 2007; Woosley & Kasen 2011). In the DE scenario, the HVFs are suggested to generate in a dense shell of basically unburned material, formed either at the outermost layer of the ejecta or CSM (Gerardy et al. 2004; Mazzali et al. 2005b; Mulligan et al. 2015; Tanaka et al. 2006, 2008). In the IE scenario, a small amount of H in the outermost layer serve as a source of free electrons, which thus suppresses the ionization status of Ca and Si through recombination. It then leads to a larger amount of Ca II and Si II, potentially producing the HVFs (Mazzali et al. 2005a; Tanaka et al. 2008). This may happen either as a contamination of H in the WD surface before the explosion or due to an interaction between the ejecta and the H-rich CSM as is similar to the DE scenario.

In our previous study (Zhao et al. 2015), the HVF of Si II $\lambda 6355$ is compared with that of Ca II NIR which is much stronger (the difference in strength could be understood as coming from different ionization potentials and oscillator strengths of the two lines). Also we found anti-correlation with $\Delta m_{15}(B)$, namely slower-declining (or brighter) SNe Ia tend to show more prominent HVFs. In this work, we further examine the behavior and correlations of the fuel-indicative O I $\lambda 7773$ absorption feature. Here we summarize our findings in relation to the expectations from the DE, AE, and IE scenarios.

(1) Mutual correlations of the velocities of HVFs, and their time evolutions: (a) The velocities of Si-HVF are about $4,000 \text{ km s}^{-1}$ lower than the velocities of the Ca-HVF, i.e., $v_{HVF}^{Si} - v_{HVF}^{Ca} \approx 4,000 \text{ km s}^{-1}$ (see Figure 17 in Zhao et al. 2015). This may not support DE scenario of the origin of HVFs. If HVFs (of O, Si and Ca) are generated in a dense-shell (either the outermost layer of the ejecta or CSM), their (central) velocities should be roughly the same, regardless of the radiation condition, unless the shell is very thick in radial scale. But such a large-scale density enhancement is not expected in hydrodynamics. Also, the velocity of Si-HVF is much lower than the expectation from the CSM scenario. As Tanaka et al. (2006) pointed out, dense blobs covering the entire photosphere would result in Si II $\lambda 6355$ absorption velocities in excess of $20,000 \text{ km s}^{-1}$ which is however observed only in a few (HV) SNe (see also the discussion in Blondin et al. 2012). (b) Similarly, the time evolution of the line velocity of O-HVF as seen in Figure 3 may not support the DE scenario as the origin of HVF either. If the HVFs originates from a dense shell created by the SN-CSM interaction, one would expect nearly a constant velocity of the HVFs as a function of time since the hydrodynamical interaction is expected to create a geometrically very thin shell in which the velocity variation is at most a few percent (Chevalier 1982). While this variation in velocity is much larger than that seen in Figure 3 where the typical velocity variation is close to 20% within one week from the earliest detection.

(2) Additional HVF of O I $\lambda 7773$: as one can see from Figures 1,2, and 4, the HVF of O I $\lambda 7773$ is accompanied by additional HVF at even higher velocity (i.e., higher by $\approx 4,000 \text{ km s}^{-1}$).

Possible explanation for this doublet-HVF includes the followings: *Explanation A*– The O-HVF may be a combination of burned and unburned clumps, where the burned clumps also form the Si- and Ca-HVFs. While the detection of Si- and Ca-HVFs suggests that the burnt clumps are distributed in a large velocity space, at high velocity, the fraction of unburned clumps may be large and then the HVF-II of O I may be dominated by such unburned ones. Given the lower ionization energy for Ca II, the HVFs can be still formed for Ca II NIR triplet at higher velocities where a smaller amount of the burnt clumps exist, but not for Si II. Alternatively, we have *Explanation B*– The HVF-II of O I could be produced from carbon burning initiated by outflowing flames at higher velocities (Mazzali et al. 2005a; Maeda et al. 2008) in an asymmetric explosion or from He burning near the WD surface. The burning may also light up HVFs of Ca II NIR which has very low excitation energy at early times. However, these processes will not be the dominant factor affecting the correlation with $\Delta m_{15}(B)$ because the amount of helium or carbon near the WD surface is small. Finally, there is *Explanation C* – The HVF-II of O I could be from a shocked CSM, while the HVF-I is from the outer layers of the ejecta.

(3) Slow time evolution in the line strength of O-HVF: for the Normal SNe Ia, the absorption strength of O-HVF weakens at a much slower rate (see Figure 3) than the Si-HVF in early phases (see Figure 5 in Zhao et al. 2015). This result can not be explained by ionization effect because Si II $\lambda 6355$ has an excitation energy even lower than the O I $\lambda 7773$ (i.e., 8.12 eV vs 9.15 eV). Nor would this be easy to explain with the DE scenario. If the fast weakening of Si- and Ca-HVFs is caused by the fast declining of density in the HVF layers, then the O-HVF would also quickly weaken for the same reason. The most plausible explanation could be given by the scenario related to the AE. If the abundance of O increases towards lower velocities, then the decreasing density as a function of time could be compensated by the increasing abundance, resulting possibly in a slow evolution. In other word, if a main body of the HVF-I forming region is dominated by the burnt material and these clumps indeed become less significant for the lower velocities toward the photosphere, then the observed behavior is reproduced.

(4) Velocity-pEW correlation of O I absorption: as it can be seen from Figure 6, the line strength of O absorption (both HVF and PHO) is decreasing with increasing velocity. This anti-correlation might be explained by the fact that more complete burning of oxygen could release more energy, deriving the remained oxygen shell to move at a higher velocity. The characteristic velocity is then moved toward the higher velocities for explosions with more complete burning. Due to the loss of absorbing oxygen material, the strength of the absorption feature could then be weakened for SNe having higher velocities. This inverse correlation is fully in line of the effect from burning difference. However, it is not clear why this relation is only strong in the SNe Ia showing a signature of C II $\lambda 6580$ absorption. Possibly, it would indicate that SNe Ia showing the strong C II would form a distinct population.

(5) Correlation and Anti-correlation between absorption strengths of O-HVF and Si- or Ca-HVFs: from Figures 7 and 8, one can see that there are positive correlations between the photospheric components of O and Si (or Ca) and anti-correlations between their HVFs. These results

likely provide an evidence that the HVF and PHO component are created at different characteristic burning layers, which is required in the AE scenario. The HVFs of Si and Ca could be produced from He burning or asymmetric burnings in the outermost layers. However, this burning process is not expected to have a significant effect on SN Ia luminosity (or $\Delta m_{15}(B)$) due to the small amount of He fuel near the WD surface. Observationally, a SN may show significant deviation from the luminosity- $\Delta m_{15}(B)$ relation established for SNe Ia (Phillips 1993) if the helium burning plays an important role. On the other hand, this relation seems difficult to explain in the DE scenario, as the density of O is also enhanced in the density enhancement process. This finding does not directly support the IE scenario (as such an effect is not required in the IE), but nor reject the IE scenario.

(6) Correlation of O-HVF with $\Delta m_{15}(B)$: from Figure 9, one can see that the strength of O-HVF tends to become stronger for SNe Ia with larger $\Delta m_{15}(B)$. This tendency is opposite to that seen in the Si-HVF (see Figure 10), where stronger HVFs are only detected in SNe Ia with $\Delta m_{15}(B) < 1.3$ mag. Indeed, the behavior of the O-HVF is understandable through the general ionization effects. For the SNe Ia with higher luminosity, their outer materials should be at higher ionization stages. This reduces the number of neutral ions, thus depressing the O I line – as is observed. On the other hand, the behavior seen in Si II is difficult to understand solely from this effect – they should also be weakened for higher SN luminosity, but the observations indicate the opposite trend. A larger Si/O pEW ratio is observed in our sample for more luminous SNe Ia, a result which solidly rejects the ionization effect as a possible dominant factor.

(7) Abnormal behavior of the HV SNe Ia: note, however, the above conclusion may only apply to the SNe Ia with relatively lower expansion velocities (i.e., $v_0^{Si} < 12,500$ km s⁻¹) since the HV SNe Ia are found to show significant scatter in the mutual correlations and anti-correlations of line strengths between O and Si (or Ca). Large scatter is also seen in the pEW - $\Delta m_{15}(B)$ correlations (see Figure 9). Thus, additional mechanism may be needed to explain the formation of the HVFs seen in HV SNe Ia if the measurements of their HVFs are generic. Given that the HVFs of Si in HV SNe have higher velocities than those in Normal SNe, a possible explanation is that the burning effect is weakened as the shells move outward. As an alternative, the HVFs of HV SNe Ia might also arise from the density enhancement of outer Si shell, perhaps due to the CSM interaction. Also, we note that indeed the HV SNe Ia could come from multiple populations, one belonging intrinsically to the same population as Normal SNe (Maeda et al. 2010) and the other exploding in the younger environment than Normal SNe (Wang et al. 2013). In this case, it could be natural that the HV SNe show diversity in the HVFs as well. Nevertheless, there is one caveat that the scatter in the HV SNe Ia could merely come from the uncertainty in the fitting.

In conclusion, the different behaviors of HVFs of O and Si (or Ca), especially the anti-correlations between the HVF strengths, are most naturally explained by a scenario where the HVF regions experienced explosive oxygen burning. This result is consistent with, and indeed expected for, the AE scenario.

4.2. Constraints on Explosion Models

Besides clarifying the origin of the HVFs formed at the outermost layers of the exploding WD, our result also places a strong constraint on the still-debated explosion mechanism. The need for formation of the HVFs from nuclear burning leaves us three possible models: standard delayed detonation (Khokhlov 1991; Gamezo et al. 2005), double detonation through He accretion (Fink et al. 2010; Woosley & Kasen 2011), and violet merger of two WDs (Pakmor et al. 2011; Röpke et al. 2012; Pakmor et al. 2012).

It has been suggested that the double detonation model will produce mostly the Fe-peak elements at high velocity (Woosley & Kasen 2011) rather than intermediate mass elements (IMEs), and the C and O will not be there in the He layer. Therefore, this model is not good to explain the HVFs seen at very outer layers of the ejecta. In the case of violet mergers, the detonation can convert the bulk of the secondary WD to the IMEs. The simulation indicates that these IMEs will indeed be left in the low-velocity zone of the ejecta, with typical velocities $< 20,000 \text{ km s}^{-1}$ (Röpke et al. 2012), and no mechanism proposed so far can accelerate the IME-rich region toward the higher velocity in this scenario. In addition, for models of either double denotation or violet merger, the "surface" detonation and the resultant HVFs are controlled by the nature of the mass accretion and/or secondary star, while the main features of the SN Ia will be determined by the primary WD. Therefore, it is difficult to understand the luminosity-velocity relation shown in Figures 9 and 10 within the framework of these two models.

On the other hand, the delayed-detonation model has a natural explanation for the observed brighter-faster relation. The diversity of the outer-layer spectral features can be attributed to the difference in the transition density ρ_{tr} from deflagration to detonation in the explosion (Höflich et al. 2002; Woosley et al. 2009). In case this transition is delayed, the expansion velocities of the ejecta will decrease and the burned materials like Si (or Ca) will be less abundant at higher velocities because a significant amount of oxygen remains unburned and does not contribute to the energy production. This supports the notion that the degree of burning is an important source of spectroscopic diversity among SNe Ia in addition to the progenitor scenarios.

In the currently available MULTI-DIMENSIONAL simulations for delayed detonation models, the velocity is still limited to $\sim 20,000 \text{ km s}^{-1}$, but this velocity may be further extended once the outermost region is well resolved, and thus the higher resolution simulations may show small clumps (currently not resolved) penetrating into the outermost layer. The observed velocity distribution of O and Si and the Si/O ratio in the outer layers of the ejecta may be used to constrain the density where the transition from deflagration to detonation occurs by comparing with the predictions from models (Höflich et al. 2002; Seitenzahl et al. 2013). However, high-resolution simulations are further needed to provide a guide to connect the detailed hydrodynamic nature of the explosion and the observed properties we have found in this paper.

5. Conclusion

With a large sample of early spectra ($t \leq -7$ days), we search for the HVFs in the absorption features O I $\lambda 7773$, Si II $\lambda 6355$ and Ca II NIR triplet. Double O-HVFs are detected in early-time spectra of SNe Ia, with velocities comparable to those of the Si-HVF and Ca-HVFs, respectively. Their mutual correlations and correlations with $\Delta m_{15}(B)$ are scrutinized.

By comparing the HVFs of O I with those of Si II and Ca II, we attempt to differentiate between various scenarios on the formations of HVFs at outer layers of the exploding ejecta. From the anti-correlation between the pEWs of HVF of O I and those of Si II and Ca II, we conclude that the oxygen burning is an important contributor to the HVFs of Si and Ca at least for Normal SNe Ia (see discussion in §4.1). This evidence is against the scenario that Si/Ca HVFs are produced from primordial material (i.e., CSM), while it is in line with the abundance enhancement scenario. Considering that the HV SNe Ia tend to have distinct explosion environments (Wang et al. 2013; Zhao et al. 2015) and weaker correlations and anti-correlations between O I and Si II (or Ca II), it is possible that the formation of their HVFs is more complicated than the Normal counterparts – indeed the HV subclass may come from multiple populations either having a normal-velocity counterpart or not (Maeda et al. 2010; Wang et al. 2013), so this could complicate the analysis of the HV SNe Ia. Given that the HVFs of Si in HV SNe Ia have higher velocities than those in Normal SNe Ia, a possible explanation is that the burning effect is weakened as the shells move outward. As an alternative, the HVFs of HV SNe Ia might also arise from the density enhancement of outer Si shell, perhaps due to the CSM interaction.

Besides distinguishing the origin of HVFs, the velocities and strengths we have measured for species of C, O, Si and Ca in this paper could be used to shape a picture of the ejecta, and further constrain the explosion models. The existence of HVF-I and even HVF-II of O I $\lambda 7773$ at higher velocities indicates, the photosphere of SNe Ia is covered by oxygen materials (clumps or a separated shell) from the white dwarf and explosive carbon burning. Current observations suggest that the delayed-detonation is the favorable explosion model for at least spectroscopically normal SNe Ia with normal photospheric velocities. Numerical explosion simulations with sufficient resolution are encouraged to focus on the outermost layer to further discriminate the explosion models using the new observational indicators we have found in this paper.

We thank the anonymous referee for his/her suggestive comments to help improve the manuscript. We are grateful to the staffs of the various telescopes and observatories with which data were obtained. The work is finally supported by the Major State Basic Research Development Program (2013CB834903), the National Natural Science Foundation of China (NSFC grants 11178003, 11325313, 11403096, and 11203034), the Strategic Priority Research Program “The Emergence of Cosmological Structures” of the Chinese Academy of Sciences (grant No. XDB09000000), and the China Scholarship Council (CSC 201406210312). The work by K.M. is partly supported by JSPS Grant-in-Aid for Scientific Research (No. 26800100) and by World Premier International Research

Center Initiative (WPI Initiative), MEXT, Japan. This research has made use of the CfA Supernova Archive, which is funded in part by the US National Science Foundation through grant AST 0907903. This research has also made use of the Lick Supernova Archive, which is funded in part by the US National Science Foundation. This work was also partially Supported by the Open Project Program of the Key Laboratory of Optical Astronomy, National Astronomical Observatories, Chinese Academy of Sciences. Funding for the LJ 2.4-m telescope has been provided by CAS and the People’s Government of Yunnan Province.

REFERENCES

- Aldering, G., Antilogus, P., Bailey, S., et al. 2006, *ApJ*, 650, 510
- Blondin, S., Matheson, T., Kirshner, R. P., et al. 2012, *AJ*143, 126
- Bloom, J. S., Kasen, D., Shen, K.J., et al. 2012. *ApJ*744, L17.
- Brown, P., Dawson, K. S., Harris, D. W., et al. 2012, *ApJ*, 749, 18
- Childress, M. J., Filippenko, A. V., Ganeshalingam, M., & Schmidt, B. P., 2014, *MNRAS*, 437, 338
- Cleveland, W. S., *J. Am. Statist.* 74, 368 (1979).
- Contreras, C., Hamuy, M., Phillips, M. M., et al. 2010, *AJ*, 139, 519
- Dilday, B., Howell, D. A., Cenko, S. B., et al. 2012, *Sci*, 337, 942
- Filippenko, A. V., et al. 1992, *ApJ*, 384, L15
- Phillips, M. M., et al. 1992, *AJ*, 103, 1632
- Phillips, M. M. 1993, *ApJ*, 413, L105
- Fink, M., Hillebrandt, W., & Röpke, F. K. 2007, *A&A*, 476, 1133
- Fink, M., Röpke, F. K., Hillebrandt, W., Seitenzahl, I. R., Sim, S. A., Kromer, M. 2010, *A&A*, 514, 53
- Fisher, A., Branch, D., Hofflich, P., Khokhlov, A. 1995, *ApJ*, 447, L73
- Folatelli, G., Phillips, M. M., Morrell, N., et al. 2012, *ApJ*, 745, 74
- Folatelli, G., Morrell, N., Phillips, M. M., et al. 2013, *ApJ*, 773, 53
- Foley, R. J., et al. 2012, *ApJ*, 744, 38
- Gamezo, V. N., Khokhlov, A. M., Oran, E. S. 2005, *ApJ*, 623, 337

- Ganeshalingam, M., Li, W., Filippenko, A. V., et al. 2010, *ApJS*, 190, 418
- Gerardy, C. L., Höflich, P., Fesen, R. A., et al. 2004, *ApJ*, 607, 391
- Graham, M. L., Foley, R. J., Zheng, W., et al. 2015, *MNRAS*, 446, 2073
- Hachinger, S., Mazzali, P. A., & Benetti, S. 2006, *MNRAS*, 370, 299
- Hamuy, M., Phillips, M. M., Suntzeff, N. B., et al. 2003, *Nature*, 424, 651
- Hatano, K., Branch, D., Fisher, A., Baron, E. & Filippenko, A. V. 1999, *ApJ*, 525, 881
- Hernández, JI., G., Ruiz-Lapuente, P., Hugo, M., T., et al. 2012, *Nature*, 489, 533
- Hicken, M., Challis, P., Jha, S., et al. 2009, *ApJ*, 700, 331
- Hicken, M., Challis, P., Kirshner, R. P., et al. 2012, *ApJS*, 200, 12
- Hillebrandt, W., & Niemeyer, J. C. 2000, *ARA&A*, 38, 191
- Höflich, P., Gerardy, C., Fesen, R., and Sakai, S. 2002, *ApJ*, 568, 791
- Hsiao, E. Y., Burns, C. R. Contreras, C. et al. 2015, *A&A*, 578, 9
- Iben, I., & Tutukov, A. V. 1984, *ApJS*, 54, 355
- Jha, S. et al., 2006, *AJ*, 131, 527
- Khokhlov, A. M. 1991, *A&A*, 245, 114
- Krisciunas, K., et al. 2003, *AJ*, 125, 166
- Li W., Filippenko A. V., Treffers R. R., Riess A. G., Hu J., & Qiu Y., 2001, *ApJ*, 546, 734
- Li, W., Bloom, J. S., Podsiadlowski, P., et al. 2011, *Nature*, 480, 348
- Livne, E. & Glasner, A. S. 1990, *ApJ*, 361, 244
- Lira, P., Suntzeff, N. B., Phillips, M. M., et al., 1998, *AJ*, 115, 234
- Maeda, K., Kawabata, Koji, Mazzali, Paolo A., et al. 2008, *Sci*, 319, 1220
- Maeda, K., Benetti, S., Stritzinger, M., et al. 2010, *Nature*, 466, 82
- Maguire, K., Sullivan, M., Ellis, R. S., et al. 2012, *MNRAS*, 426, 2359
- Maguire, K., Sullivan, M., Patat, F., et al. 2013, *MNRAS*, 436, 222
- Maguire, K., Sullivan, M., Pan, Y.-C., et al. 2014, *MNRAS*, 444, 3258
- Maoz, D., Mannucci, F., & Nelemans, G. 2014, *ARA&A*, 52, 107

- Marion, G. H., Vinko, J., Wheeler, J. C., et al. 2013, *ApJ*, 777, 40
- Marion, G. H., Brown, P. J., Vinkó, J. et al. 2015, arXiv:1507.07261v2
- Matheson, T., Kirshner, R. P., Challis, P., et al. 2008, *AJ*, 135, 1598
- Mattila, S., et al. 2005, *A&A*, 443, 649
- Maund, J. R., Höflich, P., Patat, F. et al. 2010, *ApJ*, 725, L167.
- Mazzali, P. A., Benetti, S., Stehle, M., et al. 2005a, *MNRAS*, 357, 200
- Mazzali, P. A., Benetti, S., Altavilla, G., et al. 2005b, *ApJ*, 623, L37
- Mulligan, B. W. & Wheeler J. C., 2015, arXiv:1505.05145
- Nomoto, K. 1982, *ApJ*, 253, 798
- Nomoto, K., Thielemann, F. K., Yokoi, K. 1984, *ApJ*, 286, 644
- K. Nomoto, K. Iwamoto, & N. Kishimoto. 1997, *Science*, 276, 1378
- Nugent, P., Sullivan, M., Cenko, S. B., et al. 2011, *Nature*, 480, 344
- Patat, R. et al. 1996, *MNRAS*, 278, 111
- Patat, F., Chandra, P., Chevalier, R., et al. 2007, *Sci*, 317, 924
- Pakmor, R., Kromer, M., Taubenberger, S., Sim, S. A., Röpke, F. K., Hillebrandt, W. 2012, *ApJ*, 747, 10
- Pakmor, R., Hachinger, S., Röpke, F. K. & Hillebrandt, W. 2011, *A&A*, 528, A117.
- Parrent, J. T., Thomas, R. C., Fesen, R. A., et al. 2011, *ApJ*, 732, 30
- Perlmutter, S., Aldering, G., Goldhaber, G., et al. 1999, *ApJ*, 517, 565
- Riess, A. G., Filippenko, A. V., Challis, P., et al. 1998, *AJ*, 116, 1009
- Röpke, F. K., Kromer, M., Seitenzahl, I. R., et al. 2012, *ApJ*, 750, L19
- Schaefer, B. E., & Pagnotta, A. 2012, *Nature*, 481, 164
- Seitenzahl, I. R., Ciaraldi-Schoolmann, F., Röpke, F. K., et al. 2013, *MNRAS*, 429, 1156
- Shen, K. J., & Bildsten, L. 2014, *ApJ*, 785, 61
- Silverman, J. M., Foley, R. J., Filippenko, A. V., et al. 2012a, *MNRAS*, 425, 1789
- Silverman, J. M., Ganeshalingam, M., Cenko, S. B., et al. 2012b, *ApJ*, 756, L7

- Silverman, J. M., & Filippenko, A. V. 2012c, MNRAS, 425, 1917
- Silverman, J. M., Nugent, P. E., Gal-Yam, A., et al. 2013, ApJS, 207, 3
- Silverman, J. M., Vinkó, József, Marion, G. H., et al. 2015, MNRAS, 451, 1973
- Sim, S. et al. 2012, MNRAS, 420, 3003
- Sternberg, A., Gal-Yam, A., Simon, J. D., et al. 2011, Sci, 333, 856
- Stritzinger, M., et al. 2002, AJ, 124, 2100
- Stritzinger, M., et al. 2011, AJ, 142, 156
- Tanaka, M., Mazzali, P. A., Maeda, K., & Nomoto, K. 2006, ApJ, 645, 470
- Tanaka, M., Mazzali, P. A., Benetti, S., et al. 2008, ApJ, 677, 448
- Thomas, R. C., Aldering, G., Antilogus, P., et al. 2011, ApJ, 743, 27
- Wang, X., et al. 2008, ApJ, 675, 626
- Wang, X., Filippenko, A. V., Ganeshalingam, M., et al. 2009a, ApJ, 699, L139
- Wang, X., Li, W., Filippenko, A. V., et al. 2009b, ApJ, 697, 380
- Wang, X., Wang, L., Filippenko, A. V., Zhang, T., & Zhao, X. 2013, Sci, 340, 170
- Webbink, R. F., 1984, ApJ, 277, 355
- Whelan, J., & Iben, I. 1973, ApJ, 186,1007
- Woosley, S. E., & Kasen, D. 2011, ApJ, 734, 38
- Woosley, S. E., Kerstein, A. R., Sankaran, V., Aspden, A. J., & Röpke, F. K., 2009, ApJ, 704, 255
- Zhang, T., et al. 2010, PASP, 122, 1
- Zhang, J., Wang, X., Bai, J., et al. 2014, AJ, 148, 1
- Zhang, K. Wang, X., et al. 2016, ApJ, 820, 67
- Zhao, X., Wang X., Maeda, K., et al. 2015, ApJS, 220, 20

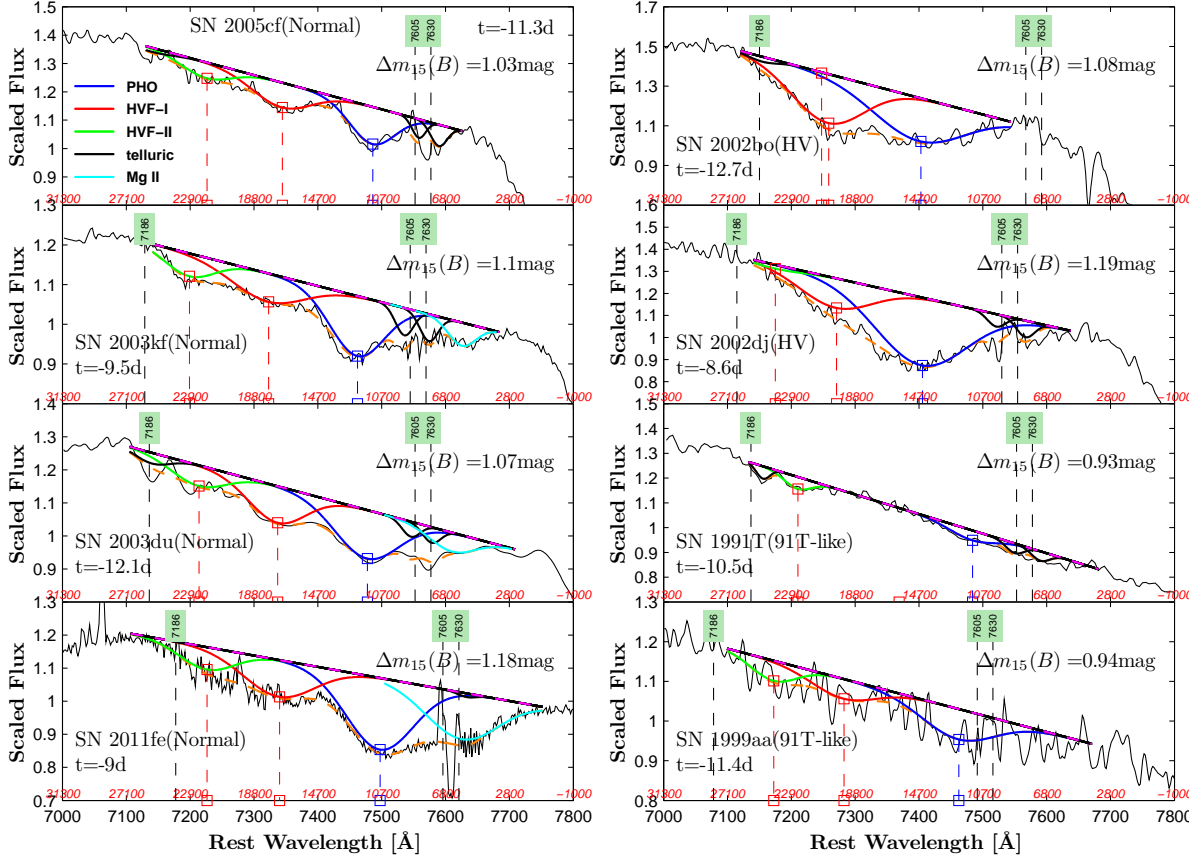


Fig. 1.— The absorption features of blueshifted O I $\lambda 7773$, centered near 7300-7500 \AA in the optical spectra, are shown for some representative SNe Ia. The SN name and the phase of the spectrum are shown in each panel. The left panels show the Normal SNe Ia in order of increasing strength (from top to the bottom) for O I $\lambda 7773$ absorption, while the right panels show the HV and 91T/99aa-like SNe Ia. Multiple gaussian fit is applied to determine different absorption components, with the blue curve representing the photospheric component, the red curve representing the main HVF (dubbed as HVF-I), and the green curve representing the the additional HVF at higher velocities (dubbed as HVF-II). The orange-color curve represents the combined fits. The vertical dashed lines mark the positions of absorption minima of the photospheric components and two HVF components. The black dashed lines mark the positions of telluric absorptions (corrected for the redshift of the supernovae) at 7186 \AA , 7605 \AA , and 7630 \AA . The number in the bracket represents the B-band magnitude decline rate over the first 15 days after the maximum light (see text for references).

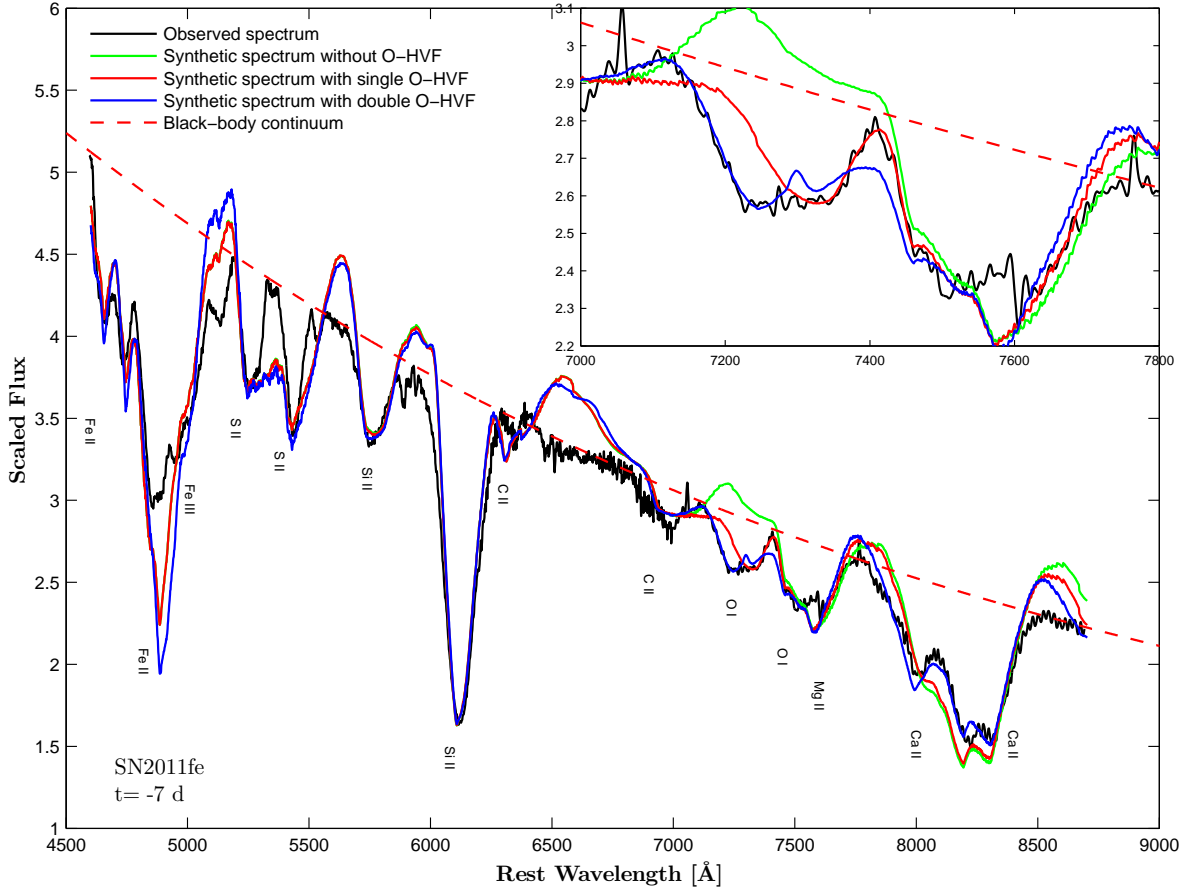


Fig. 2.— The $t = -7$ day spectrum of SN 2011fe is compared with the synthetic spectrum from the SYNOW fit (Fisher et al. 1995). The green curve represents the synthetic spectrum without including the O-HVF; the red curve represents the fit with single O-HVF; the blue curve represents the fit with double O-HVFs at $18,000 \text{ km s}^{-1}$ and $22,000 \text{ km s}^{-1}$, respectively.

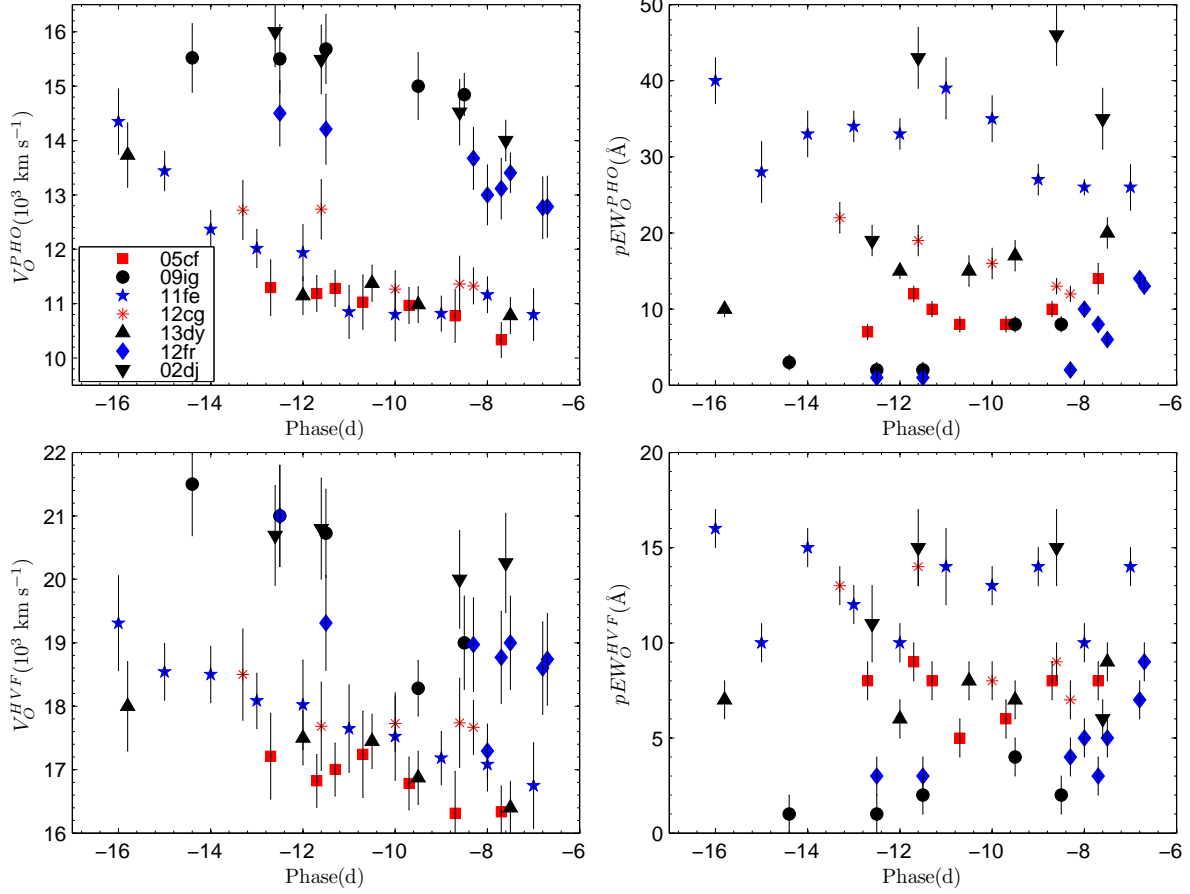


Fig. 3.— Left panels: Evolution of the absorption strength of HVF and PHO component of O I $\lambda 7773$ for some well-observed SNe Ia such as SNe 2002dj, 2005cf, 2009ig, 2011fe, 2012cg, 2012fr and 2013dy. Right panels: Similar evolutions but for the absorption strength of the HVF and PHO components of O I line.

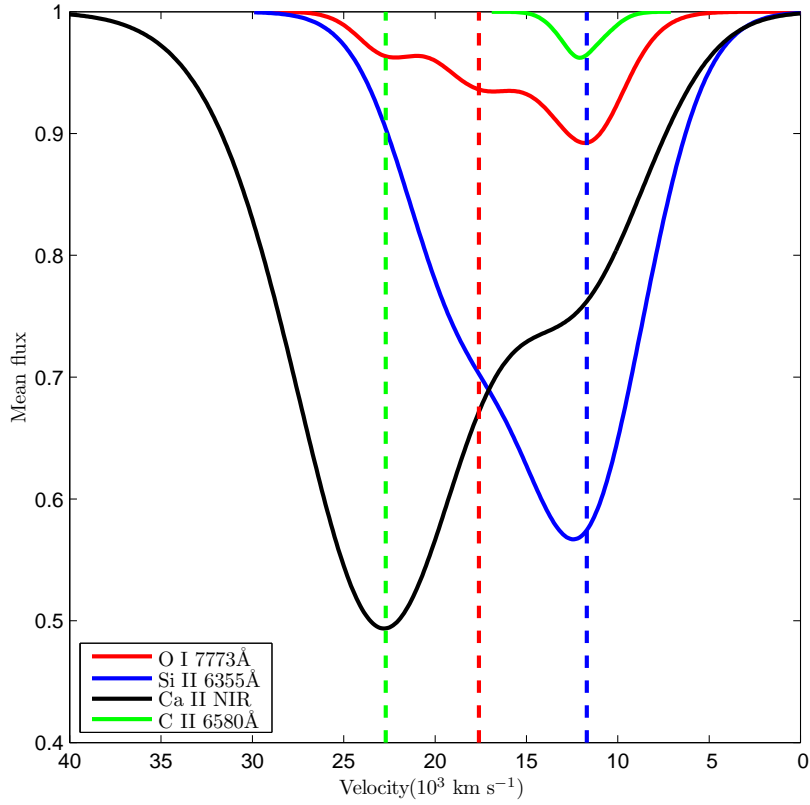


Fig. 4.— The mean line profiles of C II λ 6580 (cyan), Si II λ 6355 (blue), O I λ 7773 (red), and Ca II NIR triplet (black) absorption features, obtained with the $t \sim -10$ day spectra of spectroscopically normal SNe Ia, are shown in velocity space. The vertical dashed line marks the position of the absorption minima of HVFs and photospheric component.

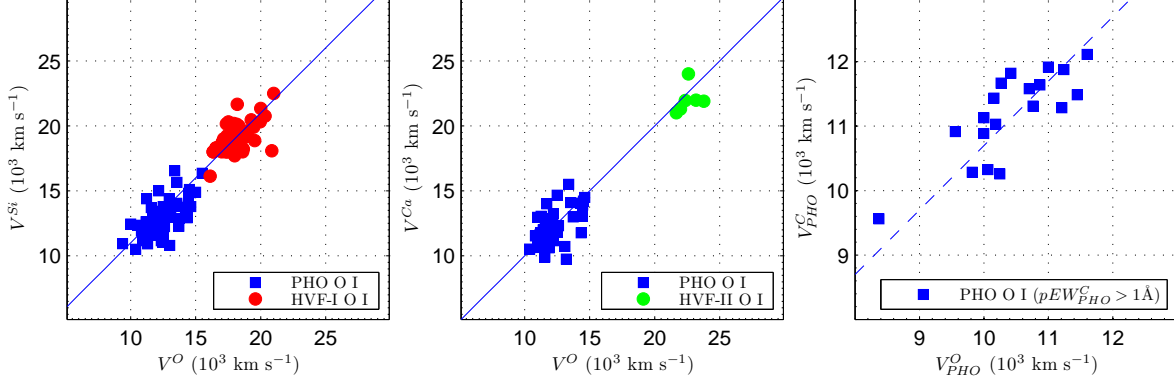


Fig. 5.— Comparison of velocity inferred from O I line with those from Si II, Ca II, and C II lines. The blue dots represent the velocity of the photospheric components. The red dots show the Si-HVF and O-HVF-I, while the green dots show the Ca-HVF and the O-HVF-II. Only those with significant detection of carbon signature are used for the comparison with the C II velocity.

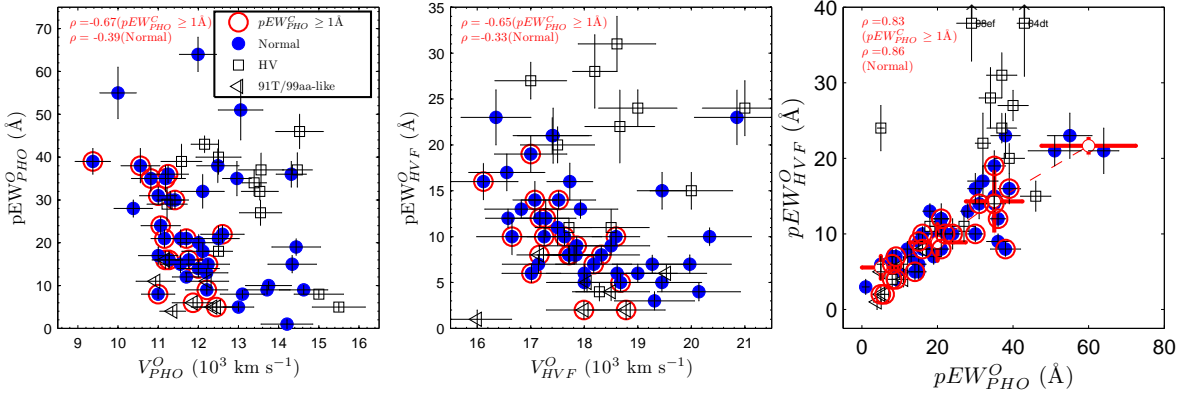


Fig. 6.— Line strength and velocity of O I $\lambda 7773$ (a) Comparison between the line strength of the photospheric component of O I $\lambda 7773$ absorption and the corresponding line velocity. (b) Similar comparison as (a) but for the line strength and velocity of the O-HVF. (c) Comparison of the line strengths between the HVF and the PHO component. Blue dots show normal SNe Ia with $v_0^{Si} < 12,500 \text{ km s}^{-1}$ at maximum light. The high-velocity SNe Ia ($v_0^{Si} \gtrsim 12,500 \text{ km s}^{-1}$ at maximum light) and the 91T/99aa-like SNe Ia are represented with squares and triangles, respectively. The larger red open circles represent the subsample of SNe Ia showing prominent C II $\lambda 6580$ absorption in the early-time spectra, i.e., $pEW > 1.0\text{\AA}$ at $t \sim -10$ days.

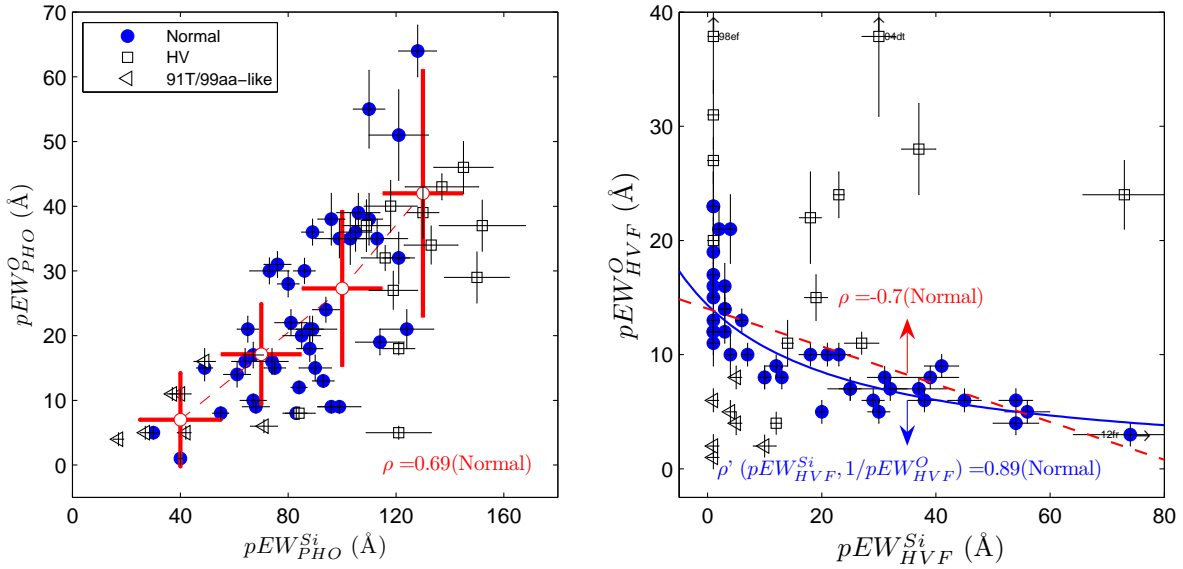


Fig. 7.— Comparison of line strength of O I $\lambda 7773$ with that of Si II $\lambda 6355$, with the left panel for the photospheric component and right panel for the HVF. The symbols are the same as in Figure 6. It is clear the PHO components of these two features show a positive correlation (with the Pearson coefficient $\rho = 0.69$) and their HVFs have an inverse correlation (with $\rho = -0.70$ for a linear correlation and $\rho = 0.89$ for a reciprocal correlation) for the subgroup of Normal SNe Ia. The open circles in the left panel represent the mean pEWs of O I $\lambda 7773$ in bins of pEWs of Si II $\lambda 6355$, and the error bars are the width of the bins and 1σ dispersion.

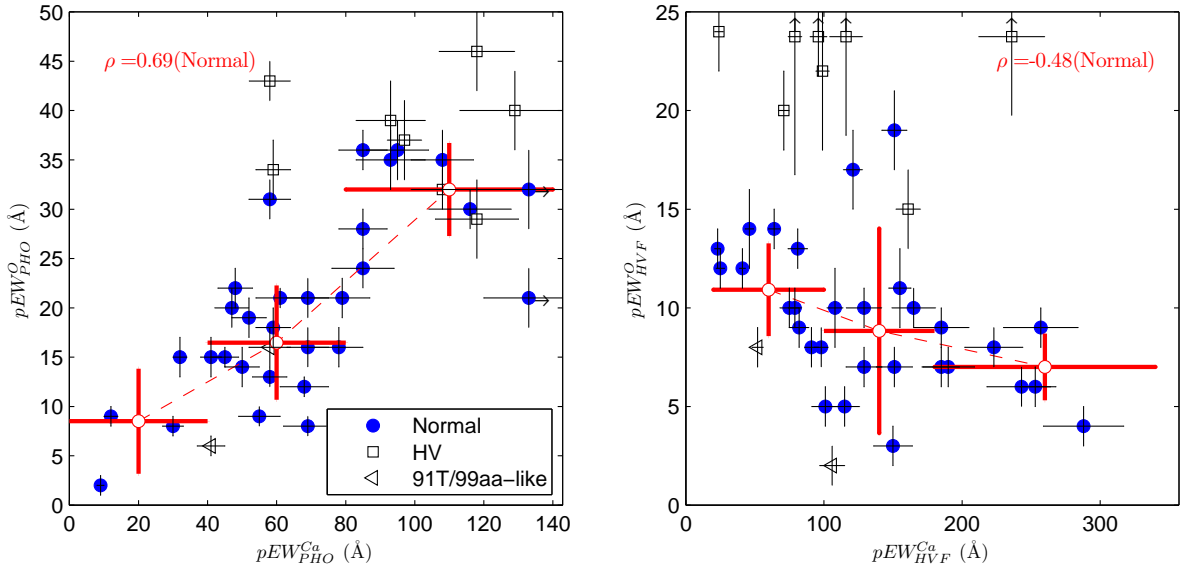


Fig. 8.— Same as Figure 7 but for the comparison with Ca II NIR triplet. Similar correlation of the PHO component and the anti-correlations of the HVFs exist between O and Ca, but are less significant compared to those seen between O and Si. The Pearson coefficients are 0.69 for the PHO-component correlation and -0.48 for the HVF anti-correlation. The symbols are the same as indicated in Figure 6.

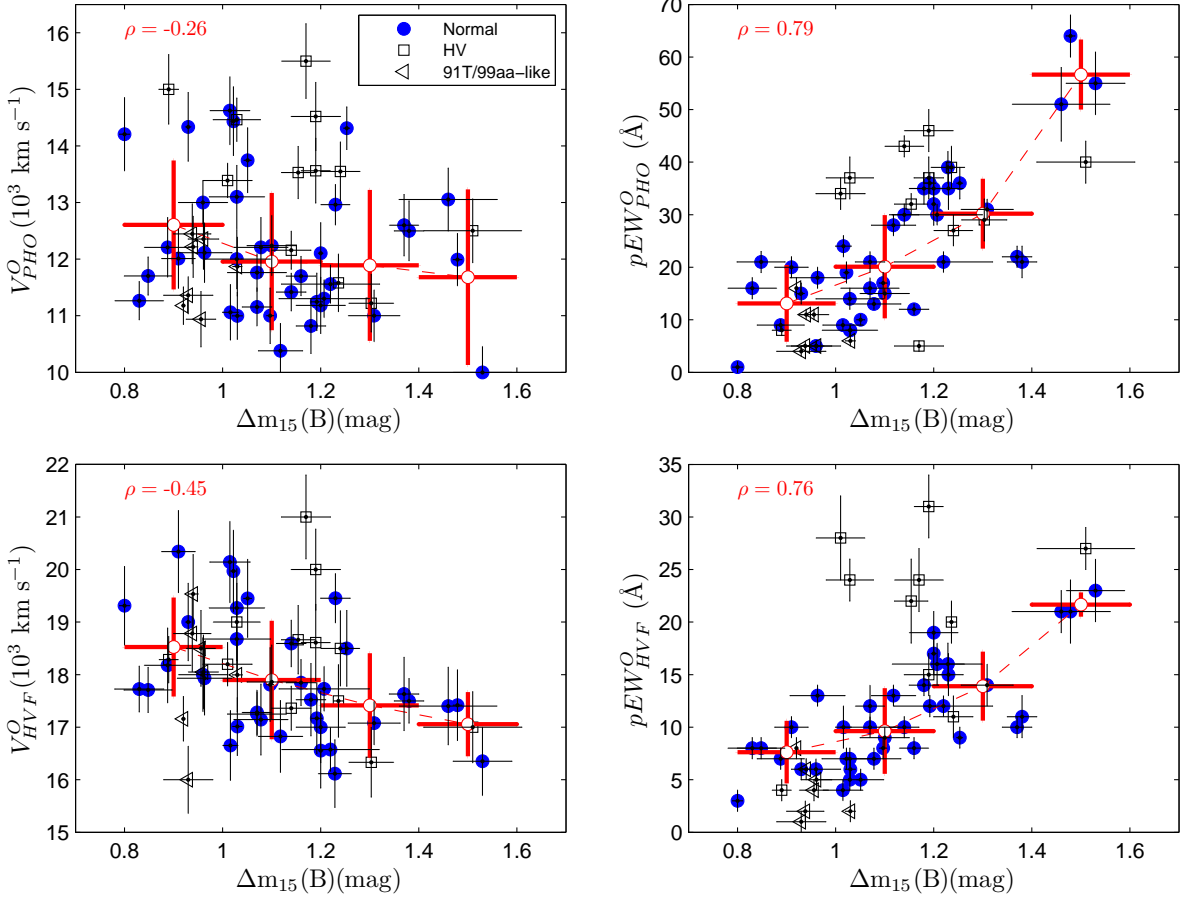


Fig. 9.— Absorption feature of O I $\lambda 7773$ as a function of the luminosity indicator $\Delta m_{15}(B)$ shown for both the PHO and the HVF components. It shows that SNe Ia with smaller $\Delta m_{15}(B)$ (or higher luminosity) tend to have larger expansion velocities (left panels) but weaker absorptions (right panels). For the PHO component (upper panels), the Pearson coefficients of these relations derived for Normal SNe Ia are -0.26 for velocity and 0.79 for line strength. For the HVF component, the corresponding coefficients are -0.45 and 0.76 for velocity and line strength, respectively. Red circles represent the mean velocity and pEWs of O I absorption in bins of $\Delta m_{15}(B)$, and the error bars represent the width of the bins and 1σ dispersion. The symbols are the same as indicated in Figure 6.

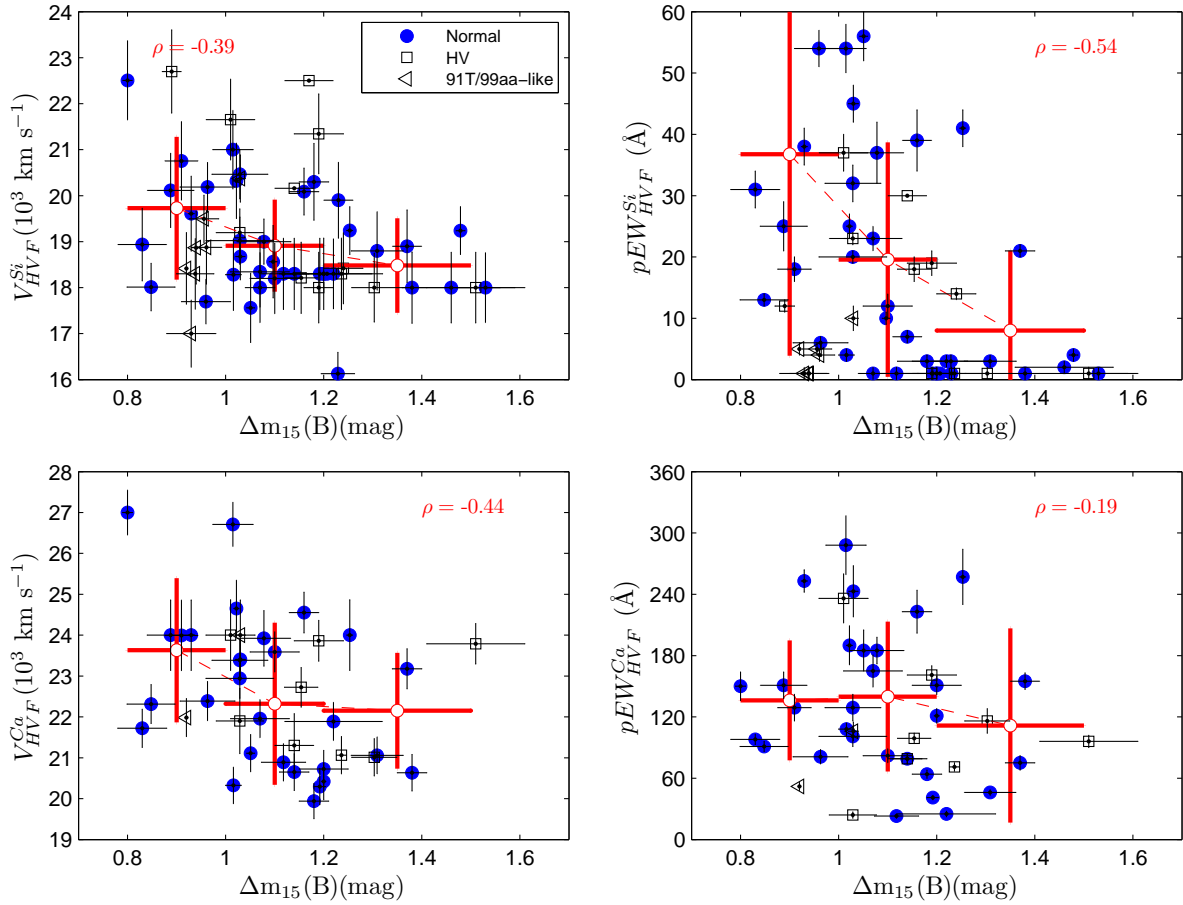


Fig. 10.— Same as Figure 9 but for correlations of the HVFs of Si II (upper panels) and Ca II (lower panels) with $\Delta m_{15}(B)$.

Table 1. Velocities and pEWs near $t \sim -10$ days

SN	O I λ 7773							Si II λ 6355					Ca II NIR				V_0^{SiP} km s $^{-1}$	$\Delta m_{15}(B)^a$ (mag)	Ref. ^r
	t ^a d	V_P^b km s $^{-1}$	W_P^c Å	V_H^d km s $^{-1}$	W_H^e Å	V_S^f km s $^{-1}$	W_S^g Å	V_P^h km s $^{-1}$	W_P^i Å	V_H^j km s $^{-1}$	W_H^k Å	V_P^l km s $^{-1}$	W_P^m Å	V_H^n km s $^{-1}$	W_H^o Å				
1991M	-7.8	12501(562)	40(4)	17000(675)	27(2)	22969(841)	3(1)	13384(624)	118(10)	18000(766)	1(1)	14672(345)	129(16)	23788(495)	96(6)	12511(434)	1.51(10)	A;B;11	
1991T*	-10.5	11362(331)	4(1)	16000(643)	1(1)	22539(504)	2(1)	12500(582)	17(2)	17000(735)	1(1)	9509(476)	0.93(05)	A;B;1	
1994D	-9.5	12601(542)	22(2)	17631(697)	10(1)	21679(822)	5(1)	12249(578)	81(6)	18900(788)	21(1)	12322(322)	48(5)	23177(491)	75(7)	11021(330)	1.37(03)	A;B;1	
1997bq	-11.8	13390(302)	34(3)	18197(412)	28(4)	22603(491)	14(2)	16545(722)	133(10)	21654(878)	37(3)	15500(605)	59(5)	24000(863)	236(24)	13000(650)	1.01(05)	A;6	
1998dm	-10.9	11702(338)	21(2)	17709(429)	8(1)	22237(501)	5(1)	11715(356)	65(4)	18011(516)	13(1)	12179(319)	69(6)	22314(475)	91(5)	11058(553)	0.85(05)	A;B;8	
1998ef	-8.9	11222(509)	29(4)	16333(664)	50(5)	21660(831)	14(1)	14394(634)	150(12)	18000(748)	1(1)	11778(314)	118(12)	21011(457)	116(12)	13260(384)	1.30(05)	A;B;12	
1999aa*	-11.4	12216(539)	11(1)	19535(750)	6(1)	24103(889)	4(1)	12457(590)	40(4)	18869(791)	1(1)	10484(310)	0.94(01)	A;B;2	
1999dk	-7.7	13531(460)	32(2)	18664(651)	22(4)	23000(856)	1(1)	13818(637)	116(9)	18214(772)	18(2)	14104(352)	108(9)	22725(484)	99(5)	12500(625)	1.15(04)	B;8	
1999dq*	-9.6	12355(531)	5(1)	18051(699)	5(1)	23586(866)	5(1)	11156(552)	27(2)	18875(798)	4(1)	10939(314)	0.96(04)	A;12	
1999ee	-9.4	13000(383)	5(1)	18000(706)	6(1)	23088(509)	5(1)	10800(544)	30(2)	17694(490)	54(3)	10189(332)	0.96(05)	A;B;10	
2000dx+	-9.0	12501(349)	18(1)	17715(431)	11(1)	22738(507)	7(1)	13793(414)	121(6)	19504(520)	27(3)	12500(625)	...	B;	
2000fa	-9.1	12011(524)	20(2)	20342(779)	10(1)	26000(948)	1(1)	13391(624)	85(7)	20756(851)	18(2)	12863(330)	47(5)	23994(862)	129(13)	12106(344)	0.91(04)	A;B;8	
2001el+	-9.0	11701(347)	12(1)	17847(437)	8(1)	22760(506)	4(1)	13428(368)	84(3)	20088(511)	39(5)	14003(338)	68(7)	24553(499)	223(21)	11715(346)	1.16(03)	10	
2002cr	-7.6	9371(439)	39(3)	16117(644)	16(2)	20926(792)	2(1)	10929(328)	106(8)	16128(466)	3(1)	10017(292)	1.23(04)	A;B;11	
2002cs+	-9.0	14465(383)	37(4)	19000(736)	24(2)	23782(523)	11(2)	14816(446)	109(9)	19197(516)	23(1)	13911(346)	97(5)	21900(799)	24(3)	13982(700)	1.03(05)	A;B;8	
2002dj	-8.6	14521(602)	46(4)	20000(771)	15(2)	24000(887)	1(1)	15108(677)	145(11)	21344(868)	19(2)	14222(351)	118(11)	23862(500)	161(9)	13095(655)	1.19(05)	A;B;1	
2002er	-8.9	12962(355)	35(4)	19454(465)	15(2)	23047(512)	20(2)	14390(654)	103(8)	19900(824)	1(1)	11895(346)	1.23(03)	A;B;1	
2003U	-8.8	13054(555)	51(7)	17403(738)	21(2)	24105(891)	1(1)	12985(388)	121(11)	18000(766)	2(1)	11046(342)	1.46(10)	A;B;1	
2003cg	-8.4	11559(342)	21(2)	16576(420)	12(1)	21848(494)	5(1)	11603(350)	89(9)	18300(765)	3(1)	12000(497)	79(8)	21890(471)	25(3)	11322(326)	1.22(10)	A;10	
2003du	-12.1	11762(336)	16(2)	17250(424)	10(1)	22363(502)	6(1)	12000(581)	74(6)	18344(774)	23(2)	11466(304)	69(6)	21957(470)	165(16)	10557(306)	1.07(06)	A;B;1	
2003ek+	-10.0	12483(536)	38(4)	20853(794)	23(3)	26000(948)	22(2)	11042(330)	96(5)	18082(771)	1(1)	10832(320)	...	A;B;	
2003fa*	-9.2	10938(488)	11(1)	18500(719)	4(1)	22412(838)	4(1)	11369(336)	37(2)	19497(513)	5(1)	10357(518)	0.96(03)	A;B;4	
2003kc	-11.4	13563(573)	37(4)	18611(725)	31(3)	21409(807)	3(1)	15646(694)	152(16)	18000(767)	1(1)	12723(608)	1.19(03)	A;B;12	
2003kf	-9.5	12240(535)	15(1)	17860(710)	9(1)	23000(856)	5(1)	11998(358)	75(4)	18200(771)	12(2)	12340(323)	45(4)	23590(496)	82(7)	11444(573)	1.10(05)	A;B;1	
2004dt	-10.8	12157(335)	43(2)	17362(418)	64(7)	21983(494)	28(3)	15000(750)	137(14)	20162(1009)	30(3)	12500(512)	58(6)	21300(780)	79(5)	14110(406)	1.14(04)	A;B;C;12	
2004eo	-11.4	12500(528)	21(3)	17500(423)	11(2)	24479(502)	1(1)	11684(364)	124(10)	18000(774)	1(1)	11800(482)	144(13)	20634(445)	155(8)	10497(296)	1.38(03)	A;B;C;1	
2004ey	-8.2	12114(523)	18(2)	17930(698)	13(1)	23000(856)	2(1)	11759(352)	88(5)	20188(532)	6(1)	11474(308)	59(5)	22386(477)	81(7)	11220(324)	0.96(06)	B;C;11	
2005cf	-10.2	10999(414)	8(1)	17012(549)	6(1)	22700(678)	3(1)	11773(348)	83(4)	18674(503)	45(3)	12963(520)	69(7)	23406(492)	243(25)	10276(302)	1.03(01)	A;B;7	
2005cg+	-9.0	11555(509)	15(2)	18000(704)	5(1)	22210(831)	2(1)	12137(366)	49(3)	18661(806)	30(2)	9906(283)	32(2)	23239(489)	115(11)	11590(342)	...	A;	
2005el	-8.1	11000(460)	31(2)	17078(416)	14(2)	22511(503)	4(1)	11355(338)	76(5)	18799(857)	3(1)	11357(304)	58(6)	21059(454)	46(3)	10811(304)	1.31(06)	A;B;C;11	
2005eu*	-9.1	12447(535)	5(1)	18782(728)	2(1)	23200(862)	4(1)	11161(324)	42(2)	18300(774)	1(1)	11068(554)	0.94(04)	A;B;11	
2006X	-11.1	15500(660)	5(1)	21000(798)	24(3)	24040(527)	7(1)	16357(818)	121(13)	22500(1125)	73(8)	15577(441)	1.17(05)	A;B;C;7	

Table 1—Continued

SN	O I λ 7773					Si II λ 6355					Ca II NIR					V_0^{SiP} km s ⁻¹	$\Delta m_{15}(B)^q$ (mag)	Ref. ^r
	t ^a d	V_P^b km s ⁻¹	W_P^c Å	V_H^d km s ⁻¹	W_H^e Å	V_S^f km s ⁻¹	W_S^g Å	V_P^h km s ⁻¹	W_P^i Å	V_H^j km s ⁻¹	W_H^k Å	V_P^l km s ⁻¹	W_P^m Å	V_H^n km s ⁻¹	W_H^o Å			
2006ax ⁺	-10.6	11061(490)24(2)	16651(662)10(2)	22137(832)2(1)	12105(361)	94(5)	18281(774)	4(1)	11554(311)	85(9)	20324(446)	108(6)	10503(298)	1.02(02)	A;B;C;3			
2006dd	-12.4	11156(341)21(2)	17280(427)12(2)	22309(502)6(1)	11306(340)	88(5)	18000(765)	1(1)	10500(525)	1.07(03)	C;11			
2006dm	-7.9	10000(460)55(6)	16351(653)23(3)	21000(795)7(1)	12454(372)	110(6)	18000(765)	1(1)	11800(590)	1.53(06)	B;7			
2006dy	-11.8	10556(491)38(4)	18317(722)8(1)	22949(842)2(1)	12363(370)	110(5)	20000(827)	10(1)	10459(523)	...	B;			
2006gr	-9.2	13100(556)8(1)	19269(744)7(1)	23148(860)3(1)	13752(418)	55(3)	20465(533)	32(3)	10723(299)	30(3)	23385(492)129(13)	11492(366)	1.03(06)	A;B;4				
2006kf	-8.3	11991(460)64(4)	17418(673)21(3)	22152(830)6(1)	12953(390)	128(7)	19239(518)	4(1)	11378(322)	1.48(01)	A;B;C;12			
2006le	-8.9	12209(524)9(1)	18176(709)7(1)	23003(855)4(1)	12882(576)	68(5)	20115(806)	25(4)	11159(325)	12(2)	24000(862)151(13)	11005(342)	0.89(05)	A;B;11				
2007F*	-9.7	11868(518)6(1)	17995(702)2(1)	22964(843)2(1)	12055(348)	71(5)	20372(513)	10(2)	10617(296)	41(4)	24000(861)106(9)	11254(324)	1.03(01)	A;B;2				
2007af	-11.3	11183(496)35(3)	17000(674)19(2)	22091(829)1(1)	12629(632)	113(12)	18300(915)	1(1)	11647(318)	93(10)	20725(454)151(9)	11007(315)	1.20(05)	A;B;C;5				
2007bd	-8.1	11580(508)39(4)	17500(689)20(2)	24000(887)1(1)	13709(402)	130(6)	18300(775)	1(1)	12459(324)	93(10)	21064(457)71(4)	12557(366)	1.24(01)	A;B;C;9				
2007bm	-8.2	11246(507)36(2)	17170(676)12(1)	21473(813)5(1)	11145(334)	89(4)	18300(774)	1(1)	11064(301)	85(7)	20297(444)41(2)	10500(525)	1.19(02)	A;B;C;9				
2007ca	-10.4	11000(491)17(2)	17811(700)8(1)	23102(859)1(1)	12053(362)	67(4)	18564(786)	10(1)	11230(314)	1.10(01)	A;B;C;9			
2007le	-9.7	14623(603)9(1)	20142(776)4(1)	24000(887)2(1)	13795(637)	99(8)	21000(858)	54(4)	14500(349)	55(6)	26710(544)288(29)	12410(370)	1.01(05)	A;B;C;1				
2008ar	-9.1	12207(529)13(1)	17145(674)7(1)	21673(819)3(1)	12187(336)	93(4)	19000(492)	37(5)	13247(312)	58(5)	23921(681)185(13)	10634(316)	1.08(06)	A;B;C;8				
2008bc	-9.7	14337(606)15(2)	19000(736)6(1)	23364(865)5(1)	12933(612)	90(6)	19609(815)	38(3)	11774(327)	41(3)	24000(862)253(11)	11600(580)	0.93(01)	C;9				
2008bf	-9.5	12000(522)14(2)	18677(723)5(1)	24010(886)2(1)	12153(360)	61(5)	19023(512)	20(1)	12412(319)	50(5)	22942(486)101(10)	11466(336)	1.03(07)	A;B;C;10				
2008hv	-11.3	14314(375)36(3)	18500(721)9(1)	22505(503)2(1)	13735(424)	105(6)	19241(518)	41(3)	14062(347)	95(9)	24000(863)257(27)	10926(312)	1.25(01)	B;C;11				
2009aa	-8.7	10381(481)28(2)	16824(683)13(1)	22255(829)1(1)	10513(316)	80(4)	18300(774)	1(1)	10516(294)	85(7)	20889(454)23(2)	10000(500)	1.12(05)	C;11				
2009ab	-10.8	11303(335)30(2)	17730(428)16(2)	23107(512)5(1)	10921(547)	73(8)	18300(915)	1(1)	10839(306)	1.21(10)	C;3			
2009ig	-9.5	15000(614)8(1)	18284(440)4(1)	22689(506)6(1)	14896(668)	84(6)	22700(906)	12(1)	13400(670)	0.89(02)	B;11			
2011by	-12.4	11418(333)30(2)	18592(443)10(1)	23001(511)1(1)	12209(368)	86(4)	18300(774)	7(1)	12000(497)116(12)	20650(450)	79(5)	10300(515)	1.14(03)	D;11				
2011df ⁺	-9.0	13711(574)9(1)	18615(722)6(1)	21961(825)3(1)	12280(366)	96(5)	19500(811)	29(2)	11005(348)	...	D;			
2011fe ⁺	-10.0	10819(485)35(3)	17522(689)14(1)	22379(837)3(1)	11917(569)	99(9)	20300(835)	3(1)	11537(296)	108(9)	19939(431)64(4)	10444(529)	1.18(03)	D;12				
2012cg ⁺	-10.0	11266(338)16(2)	17726(436)8(1)	23564(517)2(1)	12278(587)	64(5)	18936(790)	31(3)	13052(334)	78(7)	21722(466)98(5)	10000(500)	0.83(05)	D;11				
2012et ⁺	-8.0	13550(525)27(3)	18500(720)11(2)	23043(948)9(1)	14051(645)	119(9)	18421(779)	14(1)	13053(408)	1.24(04)	D;11			
2012fr ⁺	-11.5	14208(645)1(1)	19312(747)3(1)	26000(948)2(1)	13400(576)	40(1)	22507(857)109(10)	13000(528)	9(1)	27000(547)150(14)	12200(611)	0.80(01)	D;2					
2013dy* ⁺	-10.0	11179(331)16(2)	17160(423)8(1)	23184(515)6(1)	11404(562)	49(4)	18417(777)	5(1)	10644(435)	58(6)	21985(464)52(4)	10300(515)	0.92(01)	D;11				
2013gs ⁺	-9.7	13748(573)10(1)	19451(741)5(1)	25227(928)1(1)	12873(608)	67(5)	17561(752)	56(4)	9756(405)	61(7)	21112(453)185(20)	12200(610)	1.05(01)	D;11				
2013gy	-9.1	12106(538)32(4)	16553(710)17(2)	21000(911)3(1)	13211(392)	121(6)	18300(775)	1(1)	12500(512)158(16)	20423(447)121(7)	11000(316)	1.20(01)	D;11					
2014J ⁺	-10.5	14438(607)19(2)	19972(775)7(1)	23500(872)3(1)	13920(632)	114(9)	20322(816)	25(2)	13043(439)	52(5)	24651(693)190(19)	12050(360)	1.02(01)	D;11				

13

Note. — Spectral parameters measured for O I $\lambda 7773$, Si II $\lambda 6355$, and Ca II NIR triplet in the $t \sim -10 \pm 2.5$ days spectra of SNe Ia. Note that the velocity, pEW, photospheric component, HVF-I, and HVF-II are abbreviated to V, W, P, H, and S, respectively. The "*" and "★" after the SN name denote the 91T-like and 99aa-like SN Ia, respectively, while the "+" marks the SNe whose spectra used for the measurements of Ca II NIR triplet and Si II $\lambda 6355$ (or O I $\lambda 7773$) are taken at slightly different epoches.

Note. — $1-\sigma$ uncertainties shown in the brackets are in units of 1 km s^{-1} for velocity, 1 \AA for equivalent width, and 0.01 mag for $\Delta m_{15}(B)$, respectively.

Note. — References: A=CfA supernova program (Matheson et al. 2008; Blondin et al. 2012); B=Berkeley Supernova Program (Silverman et al. 2012a); C=Carnegie Supernova Project (CSP Folatelli et al. 2013); D=Tsinghua Supernova Program; 1=(Hachinger et al. 2006); 2=(Lira et al. 1998); 3=(Patat et al. 1996); 4=(Jha et al. 2006); 5=(Ganeshalingam et al. 2010); 6=(Stritzinger et al. 2002); 7=(Krisciunas et al. 2003); 8=(Mattila et al. 2005); 9=(Hicken et al. 2009); 10=(Contreras et al. 2010); 11=(Wang et al. 2009a); 12=(Wang et al. 2008); 13=(Stritzinger et al. 2011); 14=(Hicken et al. 2012); 15=(Marion et al. 2013); 16=(Foley et al. 2012); 17=(Graham et al. 2015); 18=(Zhao et al. 2015); 19=(Zhang et al. 2016); 20=(Silverman et al. 2012b); 21=(Zhang et al. 2014); 22=(Zhang et al. 2010)

^aDays since B -band maximum light;

^bVelocity of O I $\lambda 7773$, for the PHO component;

^cPseudo-equivalent width of O I $\lambda 7773$, for the PHO component;

^dVelocity of O I $\lambda 7773$, for HVF-I component;

^ePseudo-equivalent width of O I $\lambda 7773$, for HVF-I component;

^fVelocity of O I $\lambda 7773$, for the HVF-II component;

^gPseudo-equivalent width of O I $\lambda 7773$, for the HVF-II component.

^hVelocity of Si II $\lambda 6355$, for the PHO component.

ⁱPseudo-equivalent width of Si II $\lambda 6355$, for the PHO component.

^jVelocity of Si II $\lambda 6355$, for the HVF component.

^kPseudo-equivalent width of Si II $\lambda 6355$, for the HVF component.

^lVelocity of Ca II IR triplet, for the PHO component.

^mPseudo-equivalent width of Ca II IR triplet, for the PHO component.

ⁿVelocity of Ca II IR triplet, for the HVF component.

^oPseudo-equivalent width of Ca II IR triplet, for the HVF component.

^pVelocity of Si II $\lambda 6355$ measured near the maximum light.

^qLight-curve parameter, B -band light-curve decline rate $\Delta m_{15}(B)$.

^rReferences for both spectra and photometry.

Table 2. Fit Results of O I λ 7773

SN	t^a d	V_P^b km s $^{-1}$	W_P^c Å	V_H^e km s $^{-1}$	W_H^e Å	V_S^f km s $^{-1}$	W_S^g Å	R_b^h
1990N	-13.9	12851(353)	11(2)	17946(419)	12(1)	21349(795)	10(2)	0
1991M	-7.8	12501(562)	40(4)	17000(675)	27(2)	22969(841)	3(1)	0.13
1991T	-10.5	11362(331)	4(1)	16000(643)	1(1)	22539(504)	2(1)	0.06
1994D	-11.1	13119(361)	15(2)	18625(444)	10(1)	21719(486)	2(1)	0
1994D	-9.5	12601(542)	22(2)	17631(697)	10(1)	21679(822)	5(1)	0
1994D	-8.5	12001(507)	26(2)	17785(675)	10(1)	22284(816)	1(1)	0
1997bq	-11.8	13390(302)	34(3)	18197(412)	28(4)	22603(491)	14(2)	0.14
1998dk	-7.1	14496(387)	23(3)	20364(479)	15(2)	23790(527)	3(1)	0.07
1998dm	-10.9	11702(338)	21(2)	17709(429)	8(1)	22237(501)	5(1)	0.08
1998ef	-8.9	11222(509)	29(4)	16333(664)	50(5)	21660(831)	14(1)	0
1999aa	-11.4	12216(539)	11(1)	19535(750)	6(1)	24103(889)	4(1)	0
1999dk	-7.7	13531(460)	32(2)	18664(651)	22(4)	23000(856)	1(1)	0.05
1999dq	-9.6	12355(531)	5(1)	18051(699)	5(1)	23586(866)	5(1)	0
1999ee	-9.4	13000(383)	5(1)	18000(706)	6(1)	23088(509)	5(1)	0.08
1999ee	-7.4	13000(378)	8(1)	18000(705)	7(1)	23025(510)	6(1)	0.12
2000dx	-9	12501(349)	18(1)	17715(431)	11(1)	22738(507)	7(1)	0
2000fa	-9.1	12011(524)	20(2)	20342(779)	10(1)	26000(948)	1(1)	0
2001el	-9	11701(347)	12(1)	17847(437)	8(1)	22760(506)	4(1)	0.09
2002bo	-12.7	14626(603)	31(3)	20507(782)	26(2)	21000(795)	1(1)	0
2002cr	-7.6	9371(439)	39(3)	16117(644)	16(2)	20926(792)	2(1)	0
2002cs	-9	14465(383)	37(4)	19000(736)	24(2)	23782(523)	11(2)	0.02
2002dj	-12.6	16000(645)	19(2)	20693(787)	11(2)	24000(887)	1(1)	0
2002dj	-11.6	15487(632)	43(4)	20799(797)	15(2)	24000(887)	1(1)	0
2002dj	-8.6	14521(602)	46(4)	20000(771)	15(2)	24000(887)	1(1)	0.06
2002dj	-7.6	14000(375)	35(4)	20258(782)	6(1)	24000(887)	2(1)	0.1
2002er	-8.9	12962(355)	35(4)	19454(465)	15(2)	23047(512)	20(2)	0.15
2002er	-7.9	13183(363)	36(3)	20520(596)	15(2)	24000(887)	8(1)	0.09
2003U	-8.8	13054(555)	51(7)	17403(738)	21(2)	24105(891)	1(1)	0
2003cg	-8.4	11559(342)	21(2)	16576(420)	12(1)	21848(494)	5(1)	0.11
2003cg	-7.4	11763(515)	22(2)	16100(647)	8(1)	22572(843)	1(1)	0.08
2003du	-12.1	11762(336)	16(2)	17250(424)	10(1)	22363(502)	6(1)	0.12
2003ek	-10	12483(536)	38(4)	20853(794)	23(3)	26000(948)	22(2)	0
2003fa	-9.2	10938(488)	11(1)	18500(719)	4(1)	22412(838)	4(1)	0
2003fa	-8.8	11009(489)	9(1)	18500(719)	4(1)	22230(833)	3(1)	0
2003kc	-11.4	13563(573)	37(4)	18611(725)	31(3)	21409(807)	3(1)	0
2003kf	-9.5	12240(535)	15(1)	17860(710)	9(1)	23000(856)	5(1)	0.09
2003kf	-8.8	12222(534)	16(2)	17651(702)	9(1)	23000(856)	4(1)	0.08
2004dt	-10.8	12157(335)	43(2)	17362(418)	64(7)	21983(494)	28(3)	0.04
2004dt	-7.8	10325(318)	35(4)	16082(407)	42(4)	21199(484)	20(2)	0
2004eo	-11.4	12500(537)	21(3)	17500(690)	11(2)	24479(948)	1(1)	0.3
2004ey	-8.2	12114(523)	18(2)	17930(698)	13(1)	23000(856)	2(1)	0.05
2005cf	-12.7	11295(513)	7(1)	17213(679)	8(1)	23592(873)	1(1)	0.12
2005cf	-11.7	11186(331)	12(1)	16824(416)	9(1)	22034(494)	4(1)	0.06
2005cf	-11.3	11281(332)	10(1)	17002(418)	8(1)	21877(492)	4(1)	0.05
2005cf	-10.7	11029(498)	8(1)	17242(681)	5(1)	23016(857)	2(1)	0.08

Table 2—Continued

SN	t^a d	V_P^b km s ⁻¹	W_P^c Å	V_H^e km s ⁻¹	W_H^e Å	V_S^f km s ⁻¹	$W_S^g R_b^h$ Å
2005cf	-9.7	10968(329)	8(1)	16782(416)	6(1)	22383(499)	3(1) 0.08
2005cf	-8.7	10774(485)	10(1)	16315(658)	8(1)	22081(831)	5(1) 0.1
2005cf	-7.7	10334(322)	14(2)	16334(410)	8(1)	21827(489)	7(1) 0.12
2005cg	-9	11555(509)	15(2)	18000(704)	5(1)	22210(831)	2(1) 0
2005el	-8.1	11000(460)	31(2)	17078(416)	14(2)	22511(503)	4(1) 0.04
2005el	-7.1	11000(480)	31(3)	17171(672)	12(1)	22067(818)	3(1) 0.03
2005el	-6.9	11000(491)	31(3)	16555(418)	12(1)	21000(488)	4(1) 0.02
2005eu	-9.1	12447(535)	5(1)	18782(728)	2(1)	23200(862)	4(1) 0
2006X	-11.1	15500(660)	5(1)	21000(798)	24(3)	24040(527)	7(1) 0
2006X	-6.8	15579(398)	14(1)	20536(474)	24(2)	24008(856)	1(1) 0
2006ax	-10.8	11500(506)	22(2)	16200(650)	9(2)	21410(812)	2(1) 0.03
2006ax	-10.4	10622(474)	25(3)	17102(674)	11(1)	22864(851)	2(1) 0
2006ax	-8.8	10493(466)	16(2)	16630(650)	12(2)	21959(795)	2(1) 0
2006dd	-12.4	11156(341)	21(2)	17280(427)	12(2)	22309(502)	6(1) 0.22
2006dm	-7.9	10000(460)	55(6)	16351(653)	23(3)	21000(795)	7(1) 0
2006dy	-11.8	10556(491)	38(4)	18317(722)	8(1)	22949(842)	2(1) 0.08
2006gr	-9.2	13100(556)	8(1)	19269(744)	7(1)	23148(860)	3(1) 0
2006kf	-8.3	11991(460)	64(4)	17418(673)	21(3)	22152(830)	6(1) 0.04
2006le	-8.9	12209(524)	9(1)	18176(709)	7(1)	23003(855)	4(1) 0
2007F	-9.7	11868(518)	6(1)	17995(702)	2(1)	22964(843)	2(1) 0
2007af	-11.3	11183(496)	35(3)	17000(674)	19(2)	22091(829)	1(1) 0.11
2007bd	-8.1	11580(508)	39(4)	17500(689)	20(2)	24000(887)	1(1) 0
2007bm	-8.2	11246(507)	36(2)	17170(676)	12(1)	21473(813)	5(1) 0.06
2007ca	-10.4	11000(491)	17(2)	17811(700)	8(1)	23102(859)	1(1) 0
2007ci	-7.1	11614(509)	50(5)	16000(643)	20(2)	22693(845)	6(1) 0
2007le	-10.4	14623(603)	6(1)	20000(766)	2(1)	24000(887)	2(1) 0
2007le	-9.7	14859(616)	9(1)	20142(776)	4(1)	24000(887)	2(1) 0
2007le	-9.5	14618(602)	15(2)	21000(797)	4(1)	24000(887)	5(1) 0
2008ar	-9.2	12414(535)	11(1)	17264(682)	10(1)	21827(820)	3(1) 0
2008ar	-9.1	12000(522)	14(1)	17026(666)	4(1)	21518(818)	3(1) 0
2008bc	-9.7	14337(606)	15(2)	19000(736)	6(1)	23364(865)	5(1) 0.09
2008bf	-9.5	12000(522)	14(2)	18677(723)	5(1)	24010(886)	2(1) 0
2008hv	-11.3	14314(375)	36(3)	18500(721)	9(1)	22505(503)	2(1) 0.2
2009aa	-8.7	10381(481)	28(2)	16824(683)	13(1)	22255(829)	1(1) 0
2009aa	-7.7	9588(450)	29(3)	16000(643)	16(2)	21621(814)	2(1) 0
2009ab	-10.8	11303(335)	30(2)	17730(428)	16(2)	23107(512)	5(1) 0.21
2009dc	-7	9000(430)	47(5)	16984(673)	14(2)	21000(795)	2(1) 0
2009ig	-14.4	15519(630)	3(1)	21500(813)	1(1)	24145(891)	1(1) 0
2009ig	-12.5	15500(630)	2(1)	21000(797)	1(1)	24192(891)	1(1) 0
2009ig	-11.5	15682(635)	2(1)	20728(694)	2(1)	24000(887)	2(1) 0
2009ig	-9.5	15000(614)	8(1)	18284(440)	4(1)	22689(506)	6(1) 0
2009ig	-8.5	14845(387)	8(1)	19000(736)	2(1)	24000(887)	3(1) 0
2011by	-12.4	11418(333)	30(2)	18592(443)	10(1)	23001(511)	1(1) 0.04
2011by	-7.3	11344(331)	18(1)	17637(430)	12(1)	22110(498)	7(1) 0.03
2011df	-9	13711(574)	9(1)	18615(722)	6(1)	21961(825)	3(1) 0

Table 2—Continued

SN	t^a d	V_P^b km s ⁻¹	W_P^c Å	V_H^e km s ⁻¹	W_H^e Å	V_S^f km s ⁻¹	W_S^g Å	R_b^h
2011fe	-16	14347(603)	40(3)	19310(749)	16(1)	24242(854)	1(1)	0
2011fe	-15	13439(363)	28(4)	18542(448)	10(1)	23389(518)	3(1)	0
2011fe	-14	12367(350)	33(3)	18500(443)	15(1)	23361(514)	2(1)	0
2011fe	-13	12015(351)	34(2)	18086(437)	12(1)	23451(517)	1(1)	0
2011fe	-12	11936(519)	33(2)	18022(706)	10(1)	22445(840)	3(1)	0
2011fe	-11	10849(486)	39(4)	17647(691)	14(2)	22611(844)	3(1)	0
2011fe	-10	10800(485)	35(3)	17522(689)	13(1)	22379(837)	2(1)	0
2011fe	-9	10819(323)	27(2)	17183(421)	14(1)	21868(492)	6(1)	0
2011fe	-8	11163(331)	26(1)	17082(420)	10(1)	21392(487)	3(1)	0
2011fe	-7	10797(476)	26(3)	16748(678)	14(1)	21663(809)	6(1)	0.01
2012cg	-13.3	12719(544)	22(2)	18500(720)	13(1)	23144(860)	1(1)	0
2012cg	-11.6	12737(544)	19(2)	17685(695)	14(1)	22200(832)	3(1)	0
2012cg	-10	11266(338)	16(2)	17726(436)	8(1)	23564(517)	2(1)	0
2012cg	-8.6	11360(513)	13(1)	17739(703)	9(1)	23356(868)	4(1)	0
2012cg	-8.3	11326(332)	12(1)	17667(429)	7(1)	23038(512)	4(1)	0
2012et	-8	13550(525)	27(3)	18500(720)	11(2)	23043(948)	9(1)	0
2012fr	-12.5	14500(599)	1(1)	21000(797)	3(1)	23269(864)	4(1)	0
2012fr	-11.5	14208(645)	1(1)	19312(747)	3(1)	26000(948)	2(1)	0
2012fr	-8.3	13672(572)	2(1)	18971(737)	4(1)	22325(855)	1(1)	0
2012fr	-8	13000(552)	10(1)	17294(425)	5(1)	21000(795)	2(1)	0
2012fr	-7.7	13116(558)	8(1)	18769(729)	3(1)	23500(871)	2(1)	0
2012fr	-7.5	13406(364)	6(1)	19000(736)	5(1)	23500(871)	3(1)	0
2012fr	-6.8	12766(567)	14(1)	18601(730)	7(1)	25802(944)	1(1)	0.03
2012fr	-6.7	12783(563)	13(1)	18740(724)	9(1)	24251(891)	3(1)	0
2013ah	-7	10083(304)	39(4)	19757(462)	18(2)	26000(948)	11(1)	0
2013dy	-15.8	13732(590)	10(1)	18000(705)	7(1)	21752(806)	1(1)	0
2013dy	-12	11147(347)	15(1)	17500(427)	6(1)	23923(526)	2(1)	0.1
2013dy	-10.5	11375(333)	15(2)	17446(427)	8(1)	23378(517)	6(1)	0.06
2013dy	-9.5	10983(328)	17(2)	16873(419)	7(1)	22990(512)	5(1)	0.09
2013dy	-7.5	10781(333)	20(2)	16400(418)	9(1)	21617(495)	5(1)	0.15
2013gs	-9.7	13748(573)	10(1)	19451(741)	5(1)	25227(928)	1(1)	0
2013gs	-8.4	13500(568)	9(1)	18638(439)	8(1)	25356(546)	2(1)	0.19
2013gs	-7.5	13200(559)	21(2)	19742(759)	9(1)	26000(948)	2(1)	0.03
2013gy	-9.1	12106(538)	32(4)	16553(710)	17(2)	21000(911)	3(1)	0.12
2014J	-11	14952(614)	19(2)	21000(797)	7(1)	24000(887)	2(1)	0
2014J	-10	13923(599)	18(2)	18943(752)	7(1)	23000(857)	4(1)	0
2014J	-7.7	13459(379)	23(2)	19514(480)	9(1)	22782(510)	1(1)	0

Note. — Spectral parameters measured for the absorption O I $\lambda 7773$ in the early spectra of SNe Ia . The abbreviations are similar to those used in Table 1, with V, W, P, H, and S representing the velocity, pEW, photospheric component, HVF-I, and HVF-II, respectively. $1\text{-}\sigma$ uncertainties shown in the bracket are in unit of 1 km s⁻¹ and 1 Å for velocity and equivalent width, respectively.

^aDays since the B -band maximum light;

^bVelocity of O I $\lambda 7773$, for the PHO component;

^cPseudo-equivalent width of O I $\lambda 7773$, for the PHO component;

^dVelocity of O I $\lambda 7773$, for HVF-I component;

^ePseudo-equivalent width of O I $\lambda 7773$, for HVF-I component;

^fVelocity of O I $\lambda 7773$, for the HVF-II component;

^gPseudo-equivalent width of O I $\lambda 7773$, for the HVF-II component.

^hThe blending ratio between the telluric lines and the photospheric component of O I $\lambda 7773$, defined as $\text{pEW}_{\text{blending}}^{\text{telluric}} / \text{pEW}_{\text{PHO}}^{\text{O}}$, where $\text{pEW}_{\text{blending}}^{\text{telluric}}$ is the pEW of the telluric absorptions that is overlapped with the photospheric O I $\lambda 7773$, and $\text{pEW}_{\text{PHO}}^{\text{O}}$ refers to the pEW of photospheric component of O I $\lambda 7773$.

Table 3. Fit Results of C II $\lambda 6580$

SN	t	V	W	SN	t	V	W	SN	t	V	W
	d	km s ⁻¹	Å		d	km s ⁻¹	Å		d	km s ⁻¹	Å
1990N	-13.9	13496(675)	8.2(0.9)	2005cf	-12.5	12048(362)	1.4(1)	2008Z	-9.4	14000(700)	7.1(0.8)
1994D	-9.5	13114(396)	3.9(1)	2005cf	-11.7	11886(362)	1.5(1)	2008bf	-9.5	12917(388)	2.7(1)
1994D	-8.5	13060(382)	4.6(1)	2005el	-8.1	12130(364)	4.2(1)	2009F	-5.8	12145(608)	6.2(0.7)
1998aq	-9.9	12072(604)	3.7(0.4)	2005el	-7.1	11791(352)	4(1)	2009dc	-7	10351(314)	5.7(1)
1998dm	-10.9	12580(629)	1.7(0.2)	2005eu	-9.7	12487(625)	2.6(0.3)	2009ig	-15	9304(466)	0.5(0.1)
1999by	-6.2	10454(523)	1.3(0.2)	2005iq	-6.4	11889(595)	3.2(0.4)	2011by	-10	12821(390)	3.1(1)
1999cp	-12	12688(635)	6.3(0.7)	2006D	-6.3	12010(601)	6.8(0.7)	2011fe	-13	11732(360)	3.2(1)
2002cr	-11.3	11007(330)	2.7(1)	2006ax	-11.1	11326(567)	5.2(0.6)	2011fe	-12	11778(354)	2.1(1)
2002cr	-7.6	10563(316)	2.4(1)	2006dd	-12.4	12436(368)	2.9(1)	2011fe	-11	11402(346)	1.9(1)
2003du	-14.1	12722(382)	2.8(1)	2006dy	-11.8	11914(362)	3.1(1)	2011fe	-10	11285(332)	3.6(1)
2003du	-12.8	12392(372)	3.9(1)	2006gz	-9.6	13622(682)	14.6(1.5)	2011fe	-9	11094(334)	2.1(1)
2003du	-12.1	12311(370)	1.9(1)	2006le	-7.9	12284(615)	3.7(0.4)	2011fe	-7	10792(324)	1.8(1)
2003du	-10.8	12221(366)	2(1)	2007F	-9.7	12640(380)	1.2(1)	2012cg	-10	12668(382)	4.9(1)
2003du	-9.9	12009(360)	2.6(1)	2007af	-11.3	12031(366)	1.2(1)	2012cg	-8.6	12400(595)	3.1(1)
2003du	-8.9	12378(372)	2(1)	2007bm	-9.3	11436(344)	2.3(1)	2012cu	-7	12150(608)	8.1(0.9)
2003kf	-9.4	12878(644)	2.4(0.3)	2007bm	-8.5	11260(342)	1.6(1)	2013dy	-15.8	>13000	>20
2004bw	-10.5	12301(616)	10.5(1.1)	2007le	-10.7	13607(681)	0.6(0.1)
2005cf	-12.7	12048(362)	1.4(1)	2008Q	-7.3	14000(700)	6.5(0.7)

Note. — Spectral parameters measured for C II $\lambda 6580$ in early spectra of SNe Ia. Velocity is abbreviated to V, and pEW is further abbreviated to W due to limited space. 1- σ uncertainties shown in brackets are in unit of 1 km s⁻¹ and 1 Å for velocity and equivalent width, respectively.